E/I unbalance and aberrant oscillation dynamics predict preclinical Alzheimer's disease

Ehtasham Javed[1], Isabel Suárez-Méndez[2,3], Gianluca Susi[2,3], Juan Verdejo Román[4], J Matias Palva[1,5], Fernando Maestú[2,6*], Satu Palva[1,7*]

1. Neuroscience Center, HiLIFE-Helsinki Institute of Life Science, University of Helsinki, Finland.

2. Center for Cognitive and Computational Neuroscience, Complutense University of Madrid, Spain.

3. Department of Structure of Matter, Thermal Physics and Electronics, Complutense University of Madrid, Spain.

4. Department of Personality, Evaluation and Psychological Treatment, University of Granada, Spain.

5. Department of Neuroscience and Biomedical Engineering, Aalto University, Espoo, Finland.

6. Department of Experimental Psychology, Cognitive Processes and Logopedy, Complutense University of Madrid, Spain.

7. Centre for Cognitive Neuroimaging, Institute of Neuroscience & Psychology, University of Glasgow, United Kingdom.

* Equally contributing authors.

Correspondence should be addressed to:

satu.palva@helsinki.fi

Abstract

Alzheimer's disease (AD) is a major cause of dementia linked with severe decrement of cognitive functions. Animal models and presence of epileptiform activity (subclinical/clinical) suggest that neuronal hyper-excitability could play a role in the continuum of AD. The prevalence of amyloid pathology is thought to impact GABAergic terminals potentially disrupting the excitatory-inhibitory (E/I) synaptic balance and causing network dysfunction and cognitive impairment. However, there is no direct neurophysiological evidence in humans of such mechanism throughout the different stages of the disease, nor reliable markers to predict its earliest manifestations (i.e., subjective cognitive decline, SCD). Here, we use novel metrics for directly testing the hypothesis that alterations in the brain temporal coordination and non-linear dynamics should reflect underlying changes in the E/I balance. To that aim, we measured brain activity with magnetoencephalography (MEG) in a cross-sectional cohort of 343 participants (116 neurotypical controls (NC), 85 SCD, and 142 MCI). We quantified non-linear dynamics as power-law long-range temporal correlations (LRTCs) in brain oscillations, a well-known proxy for brain criticality. We demonstrate that attenuations in LRTCs and changes in their spectral profile reliably dissociate NC, SCD, and MCI individuals and that such disrupted brain dynamics are caused by exacerbated excitation shifting the dynamical regime toward a supercritical phase. Additionally, we show that aberrant non-linear dynamics predict conversion from MCI to AD using data from a longitudinal cohort. Machine learning modeling with k-nearest neighbors classification demonstrated the ability of LRTCs and E/I estimates to discriminate early-stage AD patients with better accuracy than classical structural features, highlighting their potential role as early biomarkers of AD.

Keywords Alzheimer's disease (AD); Subjective cognitive decline (SCD); Mild cognitive impairment (MCI); Neuronal oscillations; Detrended fluctuation analysis (DFA); Excitation-Inhibition imbalance; Magnetoencephalography (MEG); Long-range temporal correlation (LRTC); False discovery rate; Mini-mental state evaluation (MMSE); Boston naming test (BNT); Default mode network (DMN).

Main

Alzheimer's disease (AD) is the most prevalent form of dementia and is characterized by early memory loss, and a progressive impairment in lingual, visuospatial, and executive mental functions (McKhann et al., 2011). It has been proposed that these cognitive impairments are partially due to the altered brain functional networks as evidenced by stage-specific patterns of brain network dysfunction (Babiloni et al., 2016; Blinowska et al., 2017; López-Sanz et al., 2017; Stam et al., 2007). Specifically, functional hypersynchrony estimates have been successfully used to predict disease progression from MCI to AD (Pusil et al., 2019), and this profile being found also in preclinical stages, e.g., healthy relatives of AD Patients (Ramírez-Toraño et al., 2021)or in subjects with high amyloid deposition (Nakamura et al., 2017). Most importantly, this sign has been associated with amyloid deposition (Nakamura et al., 2017; Ranasinghe et al., 2022).

These signatures of network dysfunction reported across the AD continuum could be caused by underlying changes in the neuronal excitation-inhibition (E/I) balance (Maestú et al., 2021). In particular, dysregulation of the interplay between excitatory and inhibitory circuits can arise from increased neuronal hyper-excitability putatively caused by Aβ deposition, which induce neurotoxicity to GABAergic terminals (Garcia-Marin et al., 2009). The E/I unbalance has been proposed as a mechanism for network dysfunction and cognitive impairment. In fact, therapeutic strategies that correct the E/I unbalance in animal models have shown good promise to counteract neuronal dysfunction and cell loss (Busche & Konnerth, 2016).

However, in humans, there is still not direct electrophysiological evidence of the loss of the E/I balance. Hypersynchrony as in (Pusil et al., 2019), cannot be directly associated with hyper-excitability as demonstrated in (de Haan et al., 2017) using computational models, but can be with subclinical and clinical epileptogenic activity typically found in late stages of the disease. However, in preclinical and prodromal stages, there is still a lack of a neurophysiological evidence of the E/I unbalance.

Here, we tested the hypothesis that AD continuum could be characterized by altered brain criticality, which is primarily controlled by the E/I ratio, so that brain critical dynamics emerge at balanced E/I, while an excess of inhibition or excitation leads to sub or supercritical dynamics, respectively (Plenz & Thiagarajan, 2007; Poil et al., 2012; Shew et al., 2009). Critical brain dynamics are evidenced by power-law scaling and long-range-temporal correlations (LRTCs) in oscillation amplitudes (Cocchi et al., 2017; Hardstone

et al., 2012; Linkenkaer-Hansen et al., 2001; Nikulin et al., 2012; J. M. Palva et al., 2013; Simola et al., 2017). We thus hypothesized that aberrant LRTCs and E/I imbalance could represent potential novel markers predicting early-stage AD (subjective cognitive decline, SCD and mild cognitive impairment, MCI). We derived brain criticality and E/I ratio estimates (Bruining et al., 2020) using eyes-closed resting-state magnetoencephalographic (MEG) recordings from Normal Controls (NC), SCD, and MCI participants. We firstly explored group-level differences using cross-sectional data, in SCD and MCI participants. Secondly, to further test the validity of the previous results it was analyzed conversion from MCI to AD using longitudinal data. Finally, we used a machine learning approach to classify early-stage AD patients employing brain criticality and E/I features.

Results

Demographics

Our cross-sectional dataset included 116 NC, 85 SCD, and 142 MCI participants (see Material and Methods). Neuropsychological scores (NSs), general demographics, and group-level differences are presented in Table 1. MCI participants (73.45 ± 5.44 years) were older than SCD participants (72.16 ± 5.29 years), which in turn were older than their NC peers (70.21 ± 4.38 years). There were no group differences in sex/gender. SCD and MCI participants performed worse than NC in most neuropsychological tests, although to varying degrees. In every test, SCD performance lied within a 1SD distance from the average NC performance and within the normal range of execution. Conversely, MCI participants had lower scores relative to the SCD group in all tests, demonstrating impaired performance in working memory, verbal fluency, and language function. In terms of medial temporal lobe (MTL) integrity, MCI participants showed lower volumes in all bilateral MTL regions (hippocampi, parahippocampi, and entorhinal cortices) (normalized by the estimated total intracranial volume) than both SCD and NC participants (Fig. S1). Significant differences in left hippocampal and right parahippocampal volumes between NC (higher volumes) and SCD participants (lower volumes) were no longer significant after regressing out the age confound (Fig. S1).

Our longitudinal dataset included 22 sMCI and 23 pMCI participants that were followed up every 6 months (see Material and Methods). General demographics and Mini-Mental State Examination (MMSE) (Folstein et al., 1975) scores are presented in Table 2. There were no group differences in sex/gender. At baseline, there were no group differences in age (sMCI: 71.73 ± 5.20; pMCI: 73.70 ± 3.40; $p = 0.138$, independent samples t-test) or MMSE score (sMCI: 27.45 ± 2.28; pMCI: 25.79 ± 3.34; $p = 0.067$, independent samples t-test). In the post-session, there were significant group differences in age (sMCI: 73.05 ± 4.85; pMCI: 75.87 ± 3.55; $p = 0.032$, independent samples t-test), which was expected since the duration of the follow-up depended on the individual progression. Also, pMCI participants attained worse post-session MMSE scores compared to sMCI participants (sMCI: 26.73 ± 3.06; pMCI: 23.41 ± 4.24; $p = 0.005$, independent samples t-test) and to their baseline performance (pMCI (pre-session): 25.79 ± 3.34; pMCI (post-session): 23.41 ± 4.24; $p = 0.0008$, paired t-test). Conversely, there were no significant differences on sMCI MMSE scores across sessions (sMCI (pre-session): 27.45 ± 2.28; sMCI (post-session): 26.73 ± 3.06; $p = 0.195$, paired t-test).

Attenuation of LRTCs dissociates early SCD and MCI stages

To quantify LRTCs in oscillation amplitude fluctuations we used detrended fluctuation analysis (DFA) (Hardstone et al., 2012). DFA estimates the scaling exponent of amplitude fluctuations, ranging from 0.5 and 1.0 for power-law scaling behavior and temporally correlated processes. In our study, DFA exponents were computed for each participant from parcel time-series for wavelet frequencies between 2−90 Hz and for all cortical parcels (Fig. 1a; see Material and Methods). Mean DFA exponents were then obtained by averaging the individual DFA exponents across all parcels separately for the NC, SCD, and MCI groups, illustrating a broad peak from alpha to beta-frequencies (7−30 Hz) (Fig. 1b). Significant group differences were then identified in mean DFA exponents (Fig. 1c). SCD and MCI participants showed lower DFA exponents relative to the NC group from alpha to low-gamma frequencies (7−40 Hz) (Fig. 1b) (Kruskal-Wallis test, $p < 0.05$; False Discovery Rate (FDR) corrected). Additional post hoc tests revealed differences, i.e., progressive attenuation with disease development, in DFA exponents between the NC and SCD groups (hereafter, NC-SCD) in the alpha-band (7−12 Hz), and between the SCD and MCI groups (hereafter, SCD-MCI) in the beta-band (12−22 Hz) (Fig. 1c-e, Fig. S2).

Taken that (i) AD is associated with structural changes that initially only take place in a subset of brain regions (Jack et al., 2013), and that (ii) DFA exponents seem to provide a robust measure of group differences in early-stage AD; we examined the regional specificity of this measure by testing pairwise group differences in DFA exponents at the parcel-level using the finer anatomical resolution. In line with our whole-brain results, differences in DFA exponents between the NC and MCI groups (hereafter, NC-MCI) were extensive and found in nearly all parcels in the alpha and beta bands (Fig. 2a). Conversely, NC-SCD and SCD-MCI differences showed a shifting frequency pattern across disease progression; that is, early NC-SCD differences occurred in the alpha-band, while progressing SCD-MCI differences showed a ‘shift’ towards beta frequencies, together overlapping to the observed NC-MCI differences (Fig. 2a). Region-wise, NC-MCI differences were widespread and observed for all the brain functional systems (Fig. 2b) and parcels (Fig. 2c, Fig. S3), while NC-SCD and SCD-MCI differences showed regional specificity: NC-SCD alpha-band differences were visible in the frontoparietal network (FPN), dorsal attentional network (DAN), limbic network (Lim), and visual system (Vis), whereas SCD-MCI beta-band differences were localized within the DAN, Lim, and Vis networks (Fig. 2b-c).

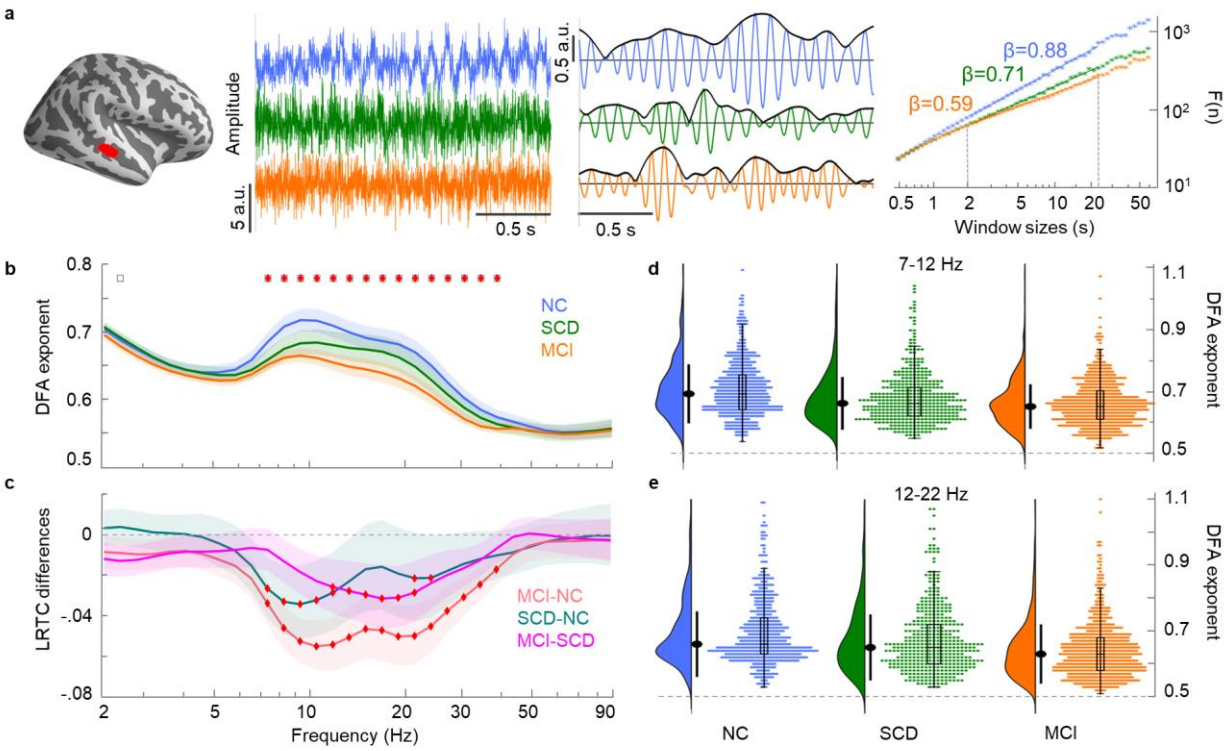

Fig. I. Between-groups averaged LRTCs differences. (**a**) Left panel: example of MEG recorded wideband time-series, one from each group (NC, SCD, and MCI), middle panel: the narrow-band (Morlet-filtered: 10.6 Hz) parcel time-series along with amplitude fluctuations from the superior temporal cortex, and right panel: their corresponding DFA exponents demonstrating group differences (see Material and Methods for details). (**b**) The averaged DFA exponent—mean of parcels (Schaefer's 400) within a subject followed by mean of subjects within groups—is represented by bright lines, while shaded regions represent bootstrapped (n=10,000) 95% confidence intervals. Non-parametric ANOVA (Kruskal-Wallis) was used to test the null hypothesis. Black-edged-squares highlight the frequencies where, with a significance level of 0.05, at least the population median of one group differed from others. The true positives after multiple comparison correction (FDR; Q=10%) are highlighted by red-diamonds. (**c**) Inter-group averaged DFA exponent differences with red-diamonds highlighting significant pairwise differences. (**d**) For 7-12 Hz, the frequencies where SCD differed from NC (in **c**), the DFA exponent distributions are shown in density-plots (equally scaled heights across groups) where the black-filled dot denotes median, and the line length represents the standard deviation. Next to the density-plots are the observed individual subject's DFA exponent values (jittered) with an overlaid boxplot. In the boxplots, the box (from bottom-to-up) denotes the first quartile, the median and third quartile, while the whiskers length represents 1.5 times the interquartile range. (**e**) Similar to **d**, the plots show the DFA exponent distributions for frequencies where SCD differed from MCI (12-22 Hz) whose averages are presented in **c**.

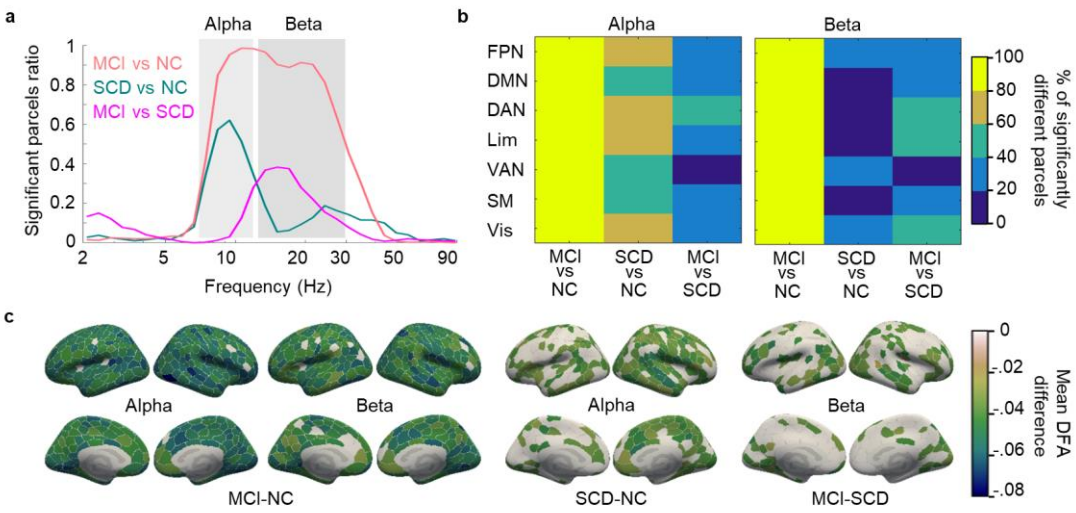

Fig. II. Parcel-level averaged pairwise LRTC differences. (**a**) Percentage of parcels (out of Schaefer's 400 parcels; see Material and Methods) found statistically different for the comparisons between NC-SCD, NC-MCI, and SCD-MCI. Wilcoxon rank-sum test was used for the statistical analysis, significance level of 0.05, at parcel-level for a given groups-pair. After multiple comparison correction using FDR (Q=20%), the ratio of significant to total parcels was computed. (**b**) Network (Yeo 7) based percentage of statistically significant parcels for the alpha and beta bands. In panel (**c)** the DFA exponent pairwise differences i.e., NC-MCI (left), NC-SCD (middle), and SCD-MCI (right) are presented on a fsaverage template for the alpha and beta bands.

To demonstrate that LRTCs provide a more robust and distinctive functional measure than the classically used spectral analysis, we also computed the power spectral densities (PSDs) of the different groups (Fig. 3a). We found significant NC-MCI and SCD-MCI differences in PSDs i.e. lower PSDs for MCI (Fig. 3b) (Kruskal-Wallis test, $p < 0.05$; FDR corrected). However, unlike in the case of DFA exponents, we could not find any NC-SCD differences. Furthermore, the averaged PSDs across the different frequency bands failed to capture the subtle differences found in the individual frequencies (Fig. 3c).

Elevated excitation characterizes disease progression

Alterations in the E/I ratio have been proposed to be the driving cause of brain network dysfunction in AD (Busche & Konnerth, 2016). Also, theoretical models of critical brain dynamics suggest that maximum (as opposed to damped) neural fluctuations occurs at the critical (as opposed to the sub or supercritical) regime (Cocchi et al., 2017; S. Palva &

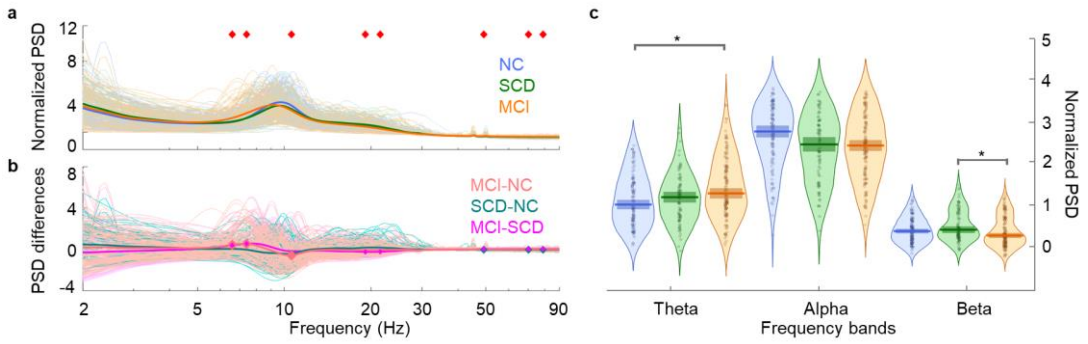

Fig. III. Group averaged power spectra. (a) For each participant, the averaged normalized PSD across parcels is plotted in dull blue, green, and orange if corresponding to the NC, SCD, and MCI groups, respectively. Individual PSDs were then averaged to get the group's mean normalized PSD, shown with brighter lines in these respective colours. Group differences (tested with Kruskal-Wallis rank-sum test and corrected for multiple comparisons via FDR (Q=10%)) are highlighted with red-diamonds. (b) Pairwise averaged differences are shown in the background for each participant. These differences were calculated in a way that, e.g., for SCD-NC, the group-averaged PSD of NC was subtracted from each subject of SCD. FDR corrected stats calculated using Wilcoxon rank sum test are highlighted with diamonds of respective pair color. In (c), the distributions of averaged PSDs across frequencies of three bands (alpha, beta, and delta) are presented along with the median (horizontal line) and 95% confidence interval (shaded rectangle) for assessment of band-wise differences.

Palva, 2018). Hence, scale-free behavior and LRTCs should peak in the critical regime, characterized by conditions of balanced E/I, and the decrease in the subcritical and supercritical phases, associated with excessive net inhibition and excitation, respectively (Fig. 4a).

To elucidate whether altered E/I balance would characterize SCD and MCI, we used a recently developed method termed *functional* E/I (*f*E/I) (Bruining et al., 2020), which quantifies an estimate of the E/I ratio from the relationship between LRTCs and the spectral power of neuronal oscillations (Fig. 4b; see Material and Methods). Using this method, we found significant (Kruskal-Wallis test, $p < 0.05$; FDR corrected) group differences in mean *f*E/I in alpha-to-gamma frequencies (Fig. 4b), similar to our findings in DFA exponents (Fig. 1b). Additional post hoc tests showed that these differences were mainly due to a significant increase of *f*E/I in the MCI relative to the NC and SCD stages.

At the parcel level, we found large NC-MCI and SCD-MCI differences, although not as robust as in DFA analysis. SCD-MCI differences were more widespread, whereas NC-SCD differences were overall weak (Fig. 4e), supporting the idea that E/I alterations echo disease progression and might represent a pathway of ongoing network disruption beginning at the SCD stage.

The healthy brain does not operate, however, at a single critical point, but rather in an extended critical regime—Griffiths phase—with large inter-individual variability (Fuscà et al., 2022; Jeong, 2004; Li et al., 2016; López-Sanz et al., 2017; López et al., 2017; Maestú & Fernández, 2020; S. Palva & Palva, 2012; Ramírez-Toraño et al., 2021; Ranasinghe et al., 2022). The theory of critical brain dynamics suggests that the covariance between scaling exponents and *f*E/I values changes with the underlying phase. For example, their correlation should be linear and positive in the subcritical phase, and linear and negative in the supercritical phase. In addition, it should follow an inverse U-shaped relationship (estimated via quadratic correlation) between regimes, so that DFA exponents peak when *f*E/I reaches a certain balance (Fig. 4a). In our population, we found that DFA exponents and *f*E/I values were mostly linearly anti-correlated across parcels, i.e., attenuated DFA exponents were associated with higher excitability (Fig. 4f; left). This result, together with findings of quadratic correlations in some parcels (Fig. 4f; right), suggests that on average the brain operates in a slightly supercritical regime. When segregated by diagnosis, we found significant linear correlations between DFA exponents and *f*E/I values in the alpha-band for SCD and MCI, but not NC participants, and significant linear correlations in the beta-band for all participants (Pearson correlation coefficient, $p < 0.05$; FDR corrected) (Fig. 4g). The identification of quadratic but not linear correlations indicates that NC participants might operate near the critical regime, while SCD and MCI participants are 'shifted' toward a supercritical phase (Fig. 4h; right), as suggested by the concurrence of quadratic and linear anti-correlations.

Aberrant LRTCs are correlated with reduced MTL volumes and neuropsychological scores

The clinical diagnosis of probable AD dementia is generally achieved through validated neuropsychological tests, while biomarker evidence (e.g., disproportionate MTL atrophy) increases the certainty of issuing a reliable diagnosis (McKhann et al., 2011). Following this, we investigated whether the aberrant brain dynamics quantified in this study were correlated with a decay in cognitive performance and MTL atrophy. We restricted the

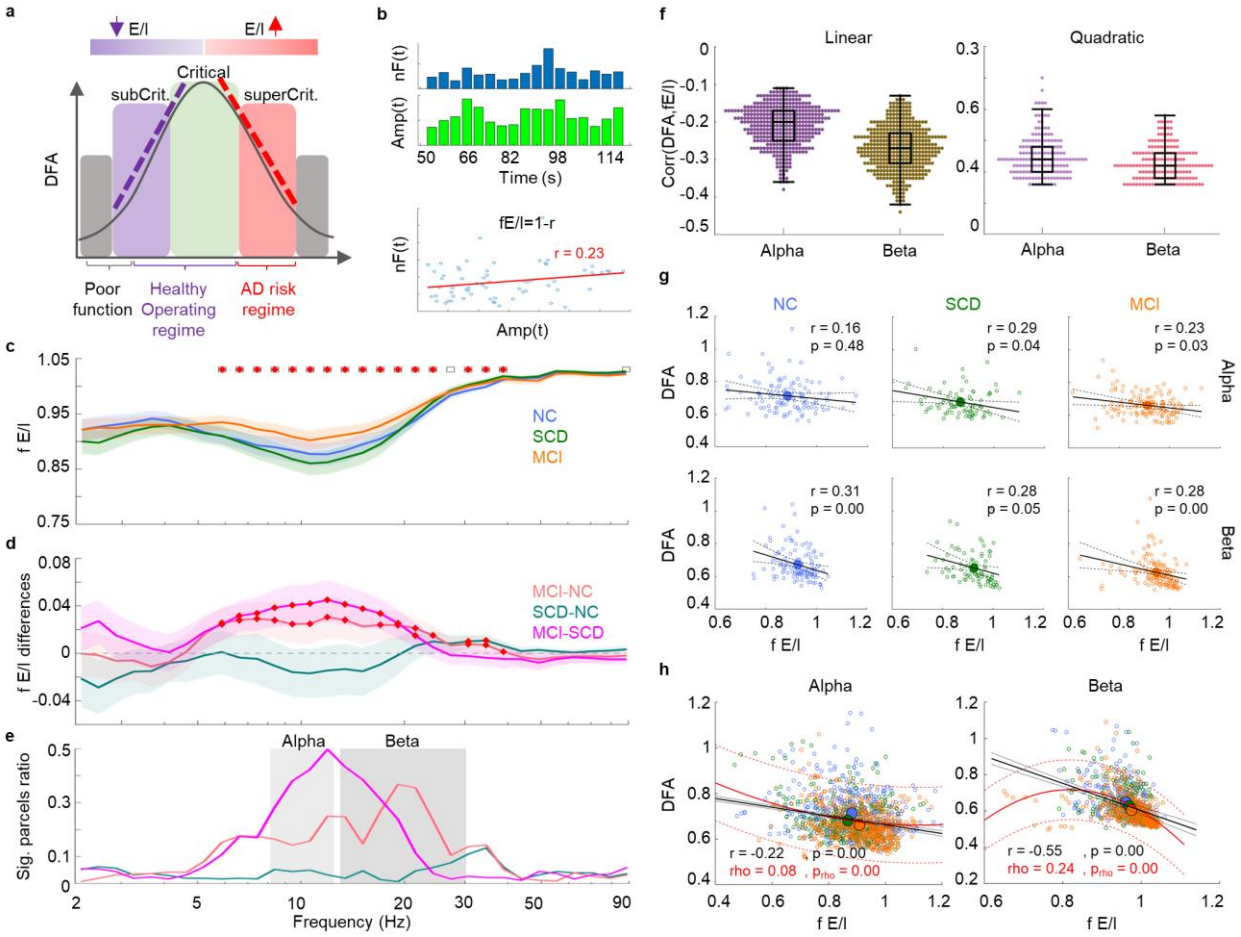

Fig. IV. Between-group fE/I differences and association with LRTCs. (**a**) Classical criticality model: an inverse U-shaped model (black-curve) represents that the fluctuations have peak LRTC when underlying neuronal activity has a certain excitatory-inhibitory (E/I) balance i.e., system at a critical state (critical or near critical state presented in green). The LRTCs decease for both types of fluctuation when underlying activity is either inhibition-dominant (subcritical regime, purple-colour; positive linear correlation between LRTC and E/I) or excitation-dominant (supercritical regime, red-colour; negative linear correlation between LRTC and E/I). The model also associates the supercritical regime with high-risk pathological function. (**b**) Normalized fluctuation function (nF(t)) and mean amplitude (Amp(t)) of each detrended signal profile, and Pearson correlation (r) between them, subtracted from 1 gives fE/I. (**c**) The group averaged fE/I values presented using bright lines (blue for NC, green for SCD, and orange for MCI) along with shaded areas describing 95% confidence interval calculated using bootstrapped (n=10,s000) method. Kruskal-Wallis rank sum provided statistical significance ($p < 0.05$, black-edged-squares) for between-groups differences. True positives using FDR (Q=10%) are marked with red-diamonds. (**d**) Group averaged pairwise differences and 95% confidence intervals in bright and shaded colors, respectively. The diamonds mark the frequencies having significant ($p < 0.05$; FDR corrected)

between-pair differences. (e) Ratio of significant parcels to Schaefer's 400 parcels for each pair (as in d) across spectra. Shaded grey areas highlight frequencies in the alpha and beta bands. In panel **f**, the linear (left) and quadratic (right) correlations between DFA exponent and fE/I across subjects. Square root of goodness of fit (r2) for quadratic correlation is computed to get the equivalent of linear correlation. Dots representing significant ($p < 0.05$; FDR (Q=10%) corrected) association for given frequency. (**g**) Linear correlation between individual groups' DFA exponent with fE/I. Dots representing significant ($p < 0.05$; FDR (Q=10%) corrected) association for the alpha and beta bands. In **h**, averaged DFA exponent and corresponding averaged fE/I values for each subject are presented for alpha (7-12 Hz) and high beta (19-30 Hz) frequencies to visualize band-wise linear and quadratic relationships. The larger filled circle represents the average across subjects for each condition.

analysis to the DFA exponents in alpha and beta-frequencies that depicted the largest group differences. We found a significant association between alpha-band DFA exponents and bilateral hippocampal (left: $r = 0.17$, $p = 0.005$; right: $r = 0.17$, $p = 0.003$), entorhinal (left: $r = 0.19$, $p = 0.001$; right: $r = 0.18$, $p = 0.004$), and parahippocampal volume (left: $r = 0.17$, $p = 0.006$; right: $r = 0.18$, $p = 0.004$) (Fig. 5a); and between beta-band DFA exponents and right entorhinal volume ($r = 0.16$, $p = 0.004$).

The correlation between DFA exponents and NSs (Table S1) was carried out at the parcel level. We found a positive correlation between alpha- and beta-band DFA exponents and memory performance (measured through nine NSs) (Fig. 5b). The topographical distribution of the correlations showed that in most parcels DFA exponents correlated with more than one NSs, revealing that these associations are not specific to one particular NS (Fig. 5c).

Classification of preclinical and prodromal AD

We showed that LRTCs and *f*E/I features provide a robust representation of group differences in early-stage AD. Next, we aimed to translate these differences into individual classifications for the different diagnostic categories of our study (NC, SCD, and MCI). This step is central for the discrimination of early-stage AD, since it has been shown that the traditional diagnosis based on NSs could be challenged, e.g., in patients with high cognitive reserve (Lojo-Seoane et al., 2018; López et al., 2017). To this aim, k-nearest neighbors (kNN) classifiers were used and trained with minimal-optimal subsets

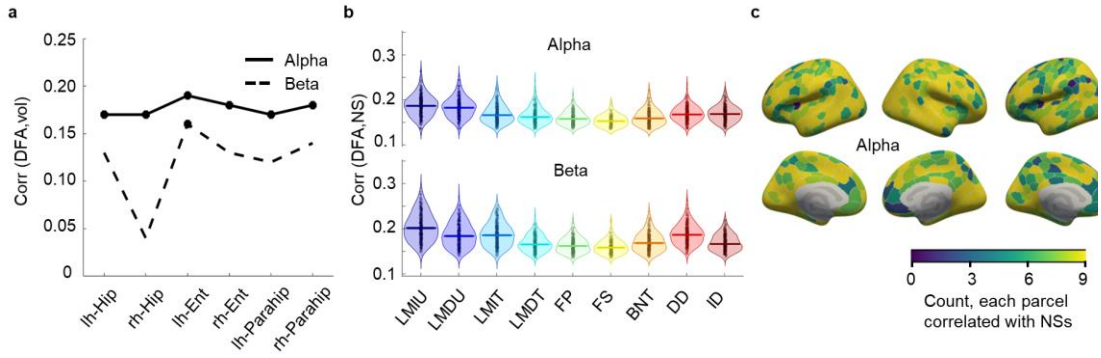

Fig. V. Correlations between LRTCs, structural, and NSs. (**a**) First of inter-modality data confluence, for differences between groups, is shown between functional (averaged alpha and beta DFA exponent) and structural measures (medial temporal lobe volumes: hippocampal, entorhinal, and para-hippocampal from both left and right hemispheres). Dots denote significant correlation (Spearman) for given regions. (**b**) Second, positive linear relationship between observed attenuations, as disease progresses, in NSs and DFA exponent for alpha (top) and beta (bottom) band) are presented for significant parcels as pirate plots. (**c**) Anatomically distributed parcels where the colour axis describes count of particular parcel that has significantly correlated with number of NSs (9 NS in total) for alpha (left) and beta (right) bands.

of functional (LRTCs and *f*E/I) and structural (MTL volumes) features, selected by the mRMR algorithm (Fig. 6a, Fig. S4a; see Material and Methods). Leave-one-out cross-validation yielded predictions of diagnostic categories greater than 80% mean accuracy across all binary problems (Fig. 6c). Importantly, SCD individuals were discriminated from both MCI and NC with high confidence (i.e., precision = 90% and 72%, recall = 80% and 84%, respectively). Similarly, the receiver operating characteristic (ROC) curves (Fig. 6d) endorsed the between-categories discriminative ability of the classifiers, with a mean area under the curve (AUC) of 0.87. We also showed that *f*E/I features were associated with higher predictive power during the early stage of the disease progression (NC-SCD), especially in theta- and gamma-bands. MTL volumes showed lower predictive power in the classification of SCD individuals when compared with NC, but became the most relevant features in the prediction of the more advanced MCI stage (Fig. 6b). We further replicated the classifications by using support vector machine (SVM) method achieving similar classification performances (see Fig. S4b-d) and demonstrating that results are robust against chosen methodology.

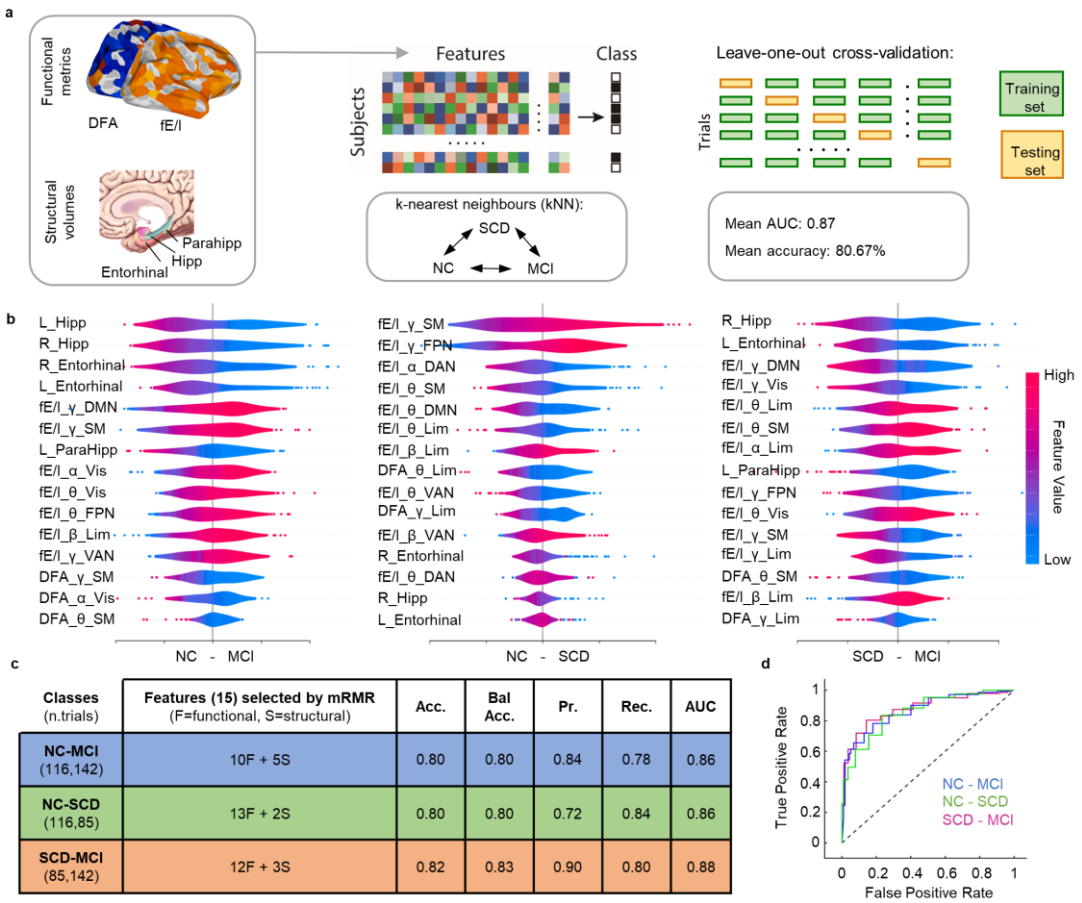

Classes (n.trials)	Features (15) selected by mRMR (F=functional, S=structural)	Acc.	Bal Acc.	Pr.	Rec.	AUC
NC-MCI (116,142)	10F + 5S	0.80	0.80	0.84	0.78	0.86
NC-SCD (116,85)	13F + 2S	0.80	0.80	0.72	0.84	0.86
SCD-MCI (85,142)	12F + 3S	0.82	0.83	0.90	0.80	0.88

Fig. VI. Classification of preclinical and prodromal AD. **(a)** Graphical summary of the functional (LRTCs and fE/I) and structural (MTL volumes) features used for classification between pairs of diagnostic categories included in the study (binary problems: NC-MCI, NC-SCD, SCD-MCI), using 3 independent kNN classifiers (k = 15). Classification was tested using leave-one-out cross-validation. **(b)** SHAP summary plots for the different binary problems (NC-MCI, left; NC-SCD, middle; SCD-MCI, right). In each summary plot, features are ranked by importance in descending order and the SHAP values measure the impact of each feature on the model output (i.e., their predictive power). The color code shows whether high (red) or low (blue) values of the feature predict the target category. For example, in the NC-SCD summary plot, gamma-band *f*E/I in the sensorimotor network is the most predictive feature of the target category SCD, and the color code shows that *high* values of that feature predict SCD. **(c)** Summary of the classification results. **(d)** ROC curve. Abbreviations: *L*, left; *R*, right; *Hipp*, hippocampus; *ParaHipp*, parahippocampus; *Entorhinal*, entorhinal cortex; θ, theta-band; α, alpha-band; β, beta-band; γ, gamma-band; *DMN*, default-mode network; *SM*, sensorimotor network; *Vis*, visual system; *FPN*, frontoparietal network; *Lim*, limbic network; *VAN*, ventral attentional network; *DAN*, dorsal attentional network.

LRTCs and fE/I differ between 'stable' and 'progressive' MCI patients

To test whether LRTCs and *f*E/I estimates would also predict disease progression within individuals, we analyzed a longitudinal dataset of MCI participants that were recorded twice (pre- and post-session). MCI participants were divided into a 'stable' (sMCI) or a 'progressive' (pMCI) group after assessing their clinical status at follow-up (see Material & Methods). DFA exponents were found to be attenuated in the pMCI relative to the sMCI already in the pre-session (Fig. 7a). Statistically significant pre-session group differences were found in alpha (7−9 Hz) and gamma (30−35 Hz) frequencies, while significant post-session group differences involved alpha (8−12 Hz) and low-beta (13−17 Hz) frequencies. Alpha-band DFA exponents were able to predict cognitive changes reflected by the MMSE through a positive linear correlation (Fig. 7b) (Spearman correlation, $p < 0.05$; FDR corrected), revealing an association between higher LRTCs and better global cognitive status.

Additionally, we found increased pre- and post-session *f*E/I in the pMCI relative to the sMCI group (Fig. 7c), suggesting that pMCI is associated with increased excitability across the alpha and gamma frequencies. This was reflected in negative linear relationship between DFA and f/EI metrics at the parcel-level in alpha and beta bands (Fig. 7d) (Spearman correlation, $p < 0.05$; FDR corrected−see Fig. S5 for significant correlations on anatomical surface) further supporting that the increased excitability being a key feature of disease progression.

The 'critical brain hypothesis' suggests that brain networks are regulated by the E/I balance so that healthy brain activity operates near a critical transition point (operate slightly subcritically to a critical point (Priesemann et al., 2014; Toker et al., 2022)).. Taken that LRTCs seem to predict disease progression from MCI to AD, we propose that SCD, MCI, and AD are associated with a progressive shift from the critical−or slightly subcritical−regime to the supercritical regime (Fig. 7e), characterized by excessive fluctuations and activity propagation that impairs network functioning and cognition. This model is consistent with the mathematical distribution of individual DFA exponents (averaged across high-theta and low-alpha (i.e. 5−7 Hz)) for the different *f*E/I values obtained from both cross-sectional and longitudinal data (Fig. 7 f-g, respectively).

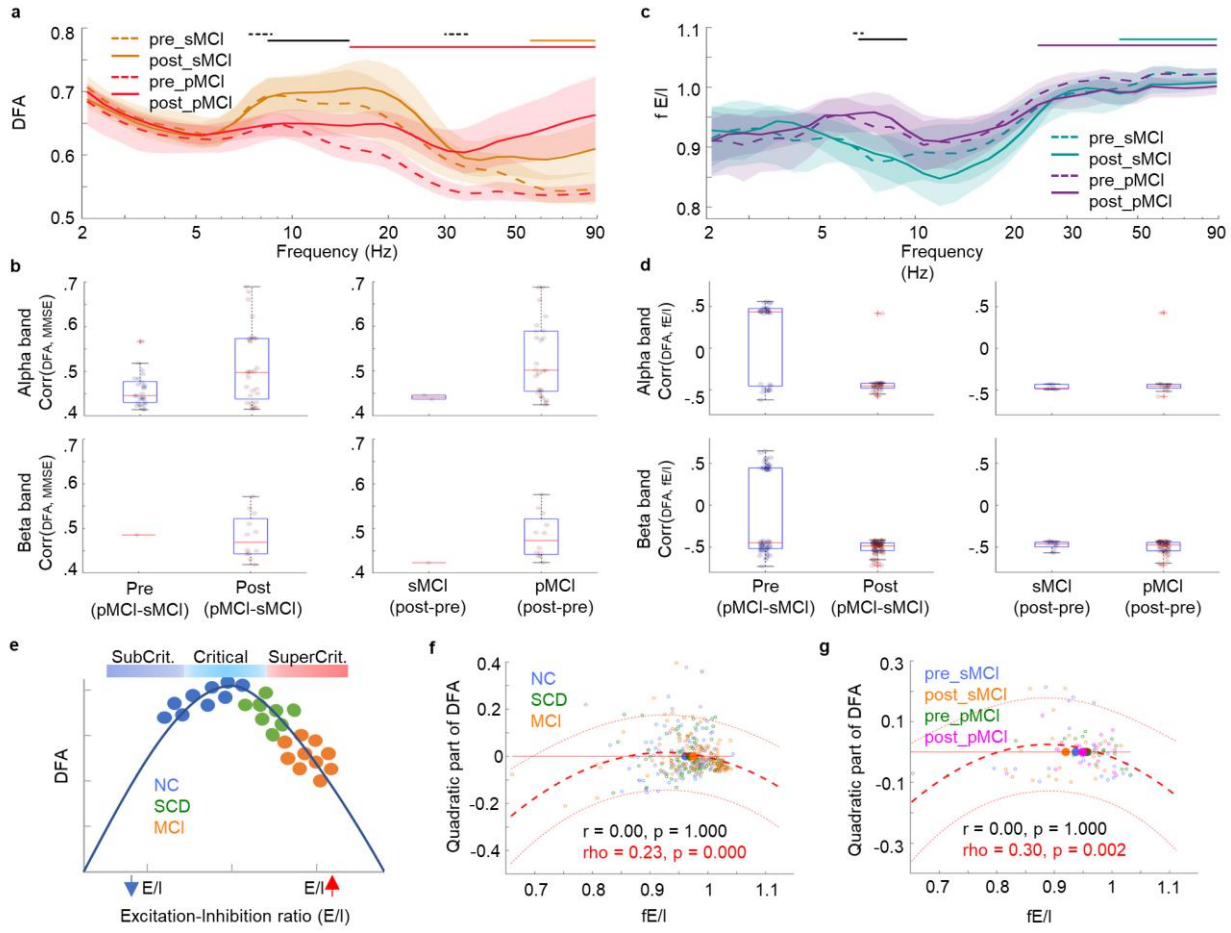

Fig. VII. Results from longitudinal data analysis. (**a**) The averaged DFA exponents, that is, mean of parcels within a subject followed by mean among subjects in respective groups (sMCI (22), pMCI (23)) for pre (doted-lines) and post (solid-lines) sessions separately, are presented and shaded regions belong to bootstrapped (n=10000) 95% confidence interval. Kruskal-Wallis rank test was used to test null hypothesis. The statistical significance in differences between groups at pre-session is given with dotted-black-lines and at post-session with solid-black-line. Between-sessions significant differences are shown with brown and red lines for sMCI and pMCI, respectively. The multiple comparison correction was done using FDR (Q=10%) method. (**b**) The inter- modality data convergence is calculated between groups difference in DFA exponents averaged across the alpha and beta bands, and groups difference in MMSE scores using Spearman correlation. The significantly correlated parcels are presented as in boxplots. (**c**) Similar to **a**, the group averaged fE/I values across spectra of 2-90 Hz are shown, and (**d**) demonstrates the association between differences between groups in DFA exponents and fE/I for the alpha and beta bands. Dots in boxplot are significantly correlated (Spearman, $p < 0.05$, FDR corrected) parcels. (**e**) Proposed theoretical model indicating disease severity-based shift from the critical−or slightly subcritical−regime to the supercritical regime and likewise demonstrated by empirical results from both cohorts in (**f**) and (**g**).

Discussion

Here, we aimed to resolve a neurophysiological pathway leading to AD and to identify how the E/I unbalance characterize early stages of the disease and if it is useful for the discrimination of early stages of AD (SCD and MCI). We analyzed LRTCs in brain oscillations amplitude fluctuations as an index of brain criticality that represents a non-linear dynamics measure of the brain state. We show that reduced LRTCs in brain oscillations allow dissociating SCD and MCI individuals from healthy age-matched controls, and also, that a frequency shift in brain dynamics from alpha to beta frequencies discriminates SCD from MCI subjects. Using longitudinal data, we demonstrated that the conversion from MCI to AD is predicted by the presence of these altered dynamics. In line with our recent hypothesis (Pusil et al., 2019), the reduction in LRTCs was associated with increased excitability and with a shift from the subcritical to the supercritical regime of the brain state. These results are vital for the understanding of AD pathophysiology with a focus on early diagnosis and intervention. In this respect, alterations in LRTCs in brain oscillations could serve as a novel biomarker for the early detection of individuals with SCD. Furthermore, since aberrant LRTCs also predicted turnover from MCI to AD, these measures could provide a clinical marker for targeting specific treatments to individuals at increased risk.

In light of the growing evidence of LRTCs being a proxy of brain criticality (Hardstone et al., 2012; Linkenkaer-Hansen et al., 2001; Nikulin et al., 2012; J. M. Palva et al., 2013; Simola et al., 2017), our findings indicate that aberrant brain critical dynamics is a key feature of early AD. This has important implications for the understanding of the electrophysiological correlates of AD, as brain criticality is regulated by a control parameter, which in the brain is primarily the E/I ratio (Plenz & Thiagarajan, 2007; Poil et al., 2012; Shew et al., 2009). Accordingly, healthy brain dynamics emerge under conditions of balanced E/I between insufficient and excessive synchronization (Beggs & Plenz, 2003; Chialvo, 2010; Haldeman & Beggs, 2005; Klaus et al., 2011; Levina et al., 2009; Poil et al., 2012; Priesemann et al., 2014), while disproportionate inhibition or excitation-leading respectively to sub or supercritical dynamics (Cocchi et al., 2017)-are associated with brain pathology (Ambrad Giovannetti & Fuhrmann, 2019; Babiloni et al., 2020; Busche & Konnerth, 2016; Meder et al., 2021).

In a recent framework, we proposed that alterations in the E/I balance lead to functional hyper-synchronization in prodromal patients of AD (X-model) (Pusil et al., 2019). This

hypothesis was supported by data from animal models of the disease (Busche & Konnerth, 2016) showing that aberrant network interactions emerge as a consequence of exacerbated brain hyperexcitability, which might be partly due to the neurotoxic effects of Aβ plaques in the proximity of GABAergic synapses (Garcia-Marin et al., 2009). For the first time, we provide evidence for this hypothesis showing that the SCD and MCI stages are associated with aberrant non-linear brain dynamics caused by increased hyperexcitability that grows throughout the disease continuum.

As brain critical dynamics are thought to be correlated with functional connectivity and oscillatory synchronization (Palva & Palva, 2012), we propose that altered brain criticality leads to aberrant electrophysiological dynamics capturing relevant AD processes both in human and animal models of AD (Babiloni et al., 2020; Maestú & Fernández, 2020) where AD patients typically exhibit a shift in the alpha peak frequency and a slowing down of brain rhythmic activity (Brassen & Adler, 2003; Jelic et al., 2000; Jeong, 2004) and regionally and spectrally specific patterns of hyper and hypo synchrony in both sensor (López-Sanz et al., 2017; Maestú et al., 2015; Shumbayawonda et al., 2020) and source-level analysis (Babiloni et al., 2016, 2017; Blinowska et al., 2017; Stam et al., 2007). Albeit MCI patients showed aberrant LRTCs in a wide range of frequencies that go from alpha to the beta bands, in line with a previously observed frequency shift in AD (Brassen & Adler, 2003; Jelic et al., 2000; Jeong, 2004), in cross-sectional analysis disease progression from SCD to MCI was associated shifted aberrant LRTCs from theta-alpha to alpha-beta bands. This shift supports the model of over excitation as in neurophysiological informed computation models increased excitation leads to shift in frequency spectrum from alpha to beta frequencies (Pinto et al., 2003).

Taken that neuronal oscillations regulate information processing and communication across distributed brain areas (Fries, 2015; Singer, 1999; Womelsdorf et al., 2014) serving fundamental roles in a variety of human sensory, motor, and cognitive functions (Fell & Axmacher, 2011; Klimesch et al., 2007; S. Palva & Palva, 2012; Schoffelen & Gross, 2009; Siegel et al., 2012; Thut et al., 2012), aberrant brain criticality is likely to lead to the variety of cognitive deficits characteristic to preclinical and clinical stages of AD. In line, the strongest aberrancies in brain critical dynamics in SCD and MCI were observed in DMN and DAN that coordinate attentional and executive functions (Corbetta et al., 2008; Power & Petersen, 2013; Smallwood et al., 2021), show alterations in functional

connectivity (López-Sanz et al., 2017; Pini, 2023) and well as the accumulation of Aβ plaques on inhibitory terminals (Buckner et al., 2009).

Previous classifications based on functional measures such as reduced oscillatory power (Fernández et al., 2013) and functional connectivity (Maestú et al., 2015) have been used to dissociate MCI from AD patients with high accuracy of 79%–83% (Pusil et al., 2019). However, until today, there has not been large sample studies dissociating SCD subjects from healthy controls or MCI subjects with such high accuracies. This discrimination capacity could be due to the use of specific metrics assessing the alterations of the non-linear dynamics at the different stages of the disease. Our results based on decoding with k-NN classifier using heterogeneous data from neuroimaging, functional and structural, demonstrated that SCD patients can be accurately classified only using brain non-linear dynamics measures while more classical functional and structural measures accurately only classified MCI but not SCD patients. These data demonstrate the importance of using heterogeneous data and machine learning for developing AD prediction models and novel prognostics (Donini et al., 2019; Janssen et al., 2018). Our results reveal a novel role of brain non-linear dynamics in initiating brain pathophysiological changes leading a pathway toward AD and demonstrate that these dynamics may serve as a novel biomarker for early and prodromal stages of AD. Additionally, the Shap plots highlight that a subset of common relevant features invert their tendencies along the different stages of disease progression, outlining a non-monotonic path. This resembles the behavior of other brain dynamics indices along the disease, as highlighted by the X-model (Pusil et al., 2019) where an analogous trajectory is found for the *phase locking value*. This behavior will be explored in more detail by the authors in future studies.

These findings could open a new window for intervention. The recovery of the E/I balance seems to be an essential target for future pharmacological interventions. In animal models the reduction of the hyperexcitability by an antiepileptic drug have led to an improvement of cognitive abilities (Sanchez et al, 2008). Furthermore, the hyperexcitability can be associated with an increased amyloid release and therefore with an increased toxicity. Non-pharmacological perspectives such as brain neuromodulation could ground their hypothesis as well in the current findings, targeting specific frequencies and E/I profiles.

Funding

This study was supported by EU Horizon 2020 framework program funding to 'The Virtual Brain Cloud (VBC) project: Personalized recommendations to neurodegenerative diseases' (https://virtualbraincloud-2020.eu /tvb-cloud-main.html) to S.P., J.M.P and F.M.

Material and Methods

Study population

The study population included 116 NC (age: 70.21 ± 4.38 years (mean ± standard deviation); females: 66.38%), 85 SCD (age: 72.16 ± 5.29 years; females: 78.82%), and 142 MCI (age: 73.45 ± 5.44 years; females: 64.79%) participants (see Table 1). SCD diagnosis was determined using the SCD-I criteria (Jessen et al., 2014): (i) self-reported cognitive concerns (mainly associated with memory); (ii) normal performance on standardized cognitive testing; (iii) feeling that the cognitive decline impairs everyday function; (iv) seeking of medical consultation; and (v) age of 60 years or more at the onset of SCD (occurring within the last 5 years). The cognitive decline was also confirmed by a reliable informant. Definitive inclusion in this group was accorded by multidisciplinary experts after discarding potential confounders of SCD (e.g., psychiatric/neurological disorders, medical conditions, prescribed drugs, or substance use). MCI diagnosis was determined using the NIA-AA guidelines for MCI due to AD (with intermediate likelihood) (Albert et al., 2011): (i) self- or informant-reported cognitive concerns; (ii) objective evidence of impairment in one or more cognitive domains; (iii) preserved independence in everyday function; (iv) absence of dementia (McKhann et al., 2011): and (v) evidence of neuronal injury (hippocampal volume measured by MRI). Besides, additional clinical tests were conducted to discard other potential causes of cognitive decline (e.g., B12 vitamin deficiency, diabetes mellitus, thyroid disease, syphilis, and human immunodeficiency virus). Participants in the NC group were cognitively healthy and did not report cognitive complaints. General exclusion criteria also involved: (i) history of psychiatric/neurological disorders, or drug consumption that could impact MEG activity (e.g., cholinesterase inhibitors); (ii) evidence of infection, infarction, or focal lesions in a T2-weighted MRI scan within 2 months to the MEG recording (rated by two independent radiologists) (Bai et al., 2012): (iii) modified Hachinski score ≥ 5; (iv) Geriatric Depression Scale-Short Form score ≥ 5; and (v) history of alcoholism/chronic use of anxiolytics, neuroleptics, narcotics, anticonvulsants, or

sedative hypnotics. A neuropsychological battery was available for all participants including Boston Naming Test (BNT) (Kaplan et al., 2001), Phonemic and Semantic Fluency Tests (Benton et al., 1983), Digit Span Test (forward and backward) and Texts of Verbal Memory of the Wechsler Memory Scale-III (Spanish version) (Wechsler, 2004). To analyze AD conversion, 45 MCI participants were followed-up every 6 months and classified according to their clinical status as 'progressive' MCI (pMCI) (if meeting the criteria for probable AD (McKhann et al., 2011) at follow-up; 23 participants; female: 60.86%) or 'stable' MCI (sMCI) (if still meeting the criteria for MCI by the end of follow-up; 22 participants; female: 63.63%) (see Table 2). All the participants were recorded over 2 MEG sessions (pre- and post-session) with an intersession interval of 1.76 ± 0.70 for the sMCI group (age: 71.73 ± 5.20 years (pre-session); 73.05 ± 4.85 years (post-session)) and 2.17 ± 1.03 for the pMCI group (age: 73.70 ± 3.40 years (pre-session); 75.87 ± 3.56 years (post-session)). Pre- and post-session MMSE scores were recorded for every participant.

All the participants were right-handed (Oldfield, 1971) and native Spanish. All the participants signed informed consent before enrolling. The study was approved by the Ethics Committee of the Hospital Clínico Universitario San Carlos and conducted according to current guidelines and regulations.

Data acquisition

Eyes-closed resting-state MEG data were recorded using a 306-channel (102 magnetometers, 204 planar gradiometers) Vectorview system (Elekta AB, Stockholm, Sweden) installed at the Center for Biomedical Technology (Madrid, Spain). MEG data were sampled at F_s =1,000 Hz with an online anti-alias band-pass filter (0.1−330 Hz). The recordings lasted from 3 to 5 minutes. Additionally, three-dimensional T1-weighted anatomical MRI scans were acquired in a 1.5 T MRI system (GE Healthcare, Chicago, Illinois) using a high-resolution antenna and a homogenization PURE filter (fast spoiled gradient echo sequence, with parameters: repetition time/echo time/inversion time = 11.2/4.2/450 ms, flip angle = 12˚, slice thickness = 1 mm, 256 × 256 matrix, and field of view = 256 mm). MRI data were collected at the Hospital Clínico Universitario San Carlos (Madrid, Spain).

MEG data pre-processing

MEG data were pre-processed in two steps at two different sites, the Complutense University of Madrid (UCM) (segmented data pre-processing) and the University of

Helsinki (UH) (continuous data pre-processing), using MATLAB and the Fieldtrip toolbox (Oostenveld et al., 2011) (https://www.fieldtriptoolbox.org/).

At the UCM, MEG recordings were processed offline using the temporally extended signal space separation method (tSSS) (Taulu & Hari, 2009) (Maxfilter software v2.2; correlation threshold = 0.9, time window = 10 s), to remove external magnetic noises, interpolate bad channels, and compensate for head motion during the recording. Next, the data were imported into MATLAB (R2017b, Mathworks, Inc.) and segmented into 4-seconds epochs of non-overlapping activity. Noisy segments of data containing muscular, ocular (blinks), or SQUID jump artifacts were first flagged using Fieldtrip's automatic artifact detection pipeline and visually corrected. Then, an independent component analysis-based (ICA) algorithm was applied to the clean segments, and artifactual components (containing noisy, ocular, or cardiac signals) were visually identified. Artifact definitions (sample points and labels), ICA transformations, and the list of artifactual ICA components were saved and used to clean the continuous data in the next step.

At the UH, the artifacts were visually re-confirmed by an independent researcher, and additional 'high-amplitude' artifacts were annotated. Data cleaning was aimed at maintaining the original length of the data and conducted in two steps: (i) continuous data were imported into MATLAB, and then projected to component space using the ICA transformation matrix. Then, the artifactual ICA components were removed from the data using Fieldtrip's *ft_rejectcomponent*, and the rest were back-projected to sensor-space; (ii) artifactual segments were cleaned using an algorithm for *data replacement* to avoid the impact of data breaks on our analyses (see (Smith et al., 2020)) and to preserve the full length of the recordings. First, artifactual sample points were replaced with NaNs and then filled with the steady trends of the signals calculated from 50 samples of pre- and post-artifact data smoothed with a Savitzky-Golay finite impulse response (FIR) filter to prevent edge effects. Finally, for each artifact, clean segments of data of the same length and from the same channel were superimposed onto its steady trends using MATLAB's *interp1*.

Source-reconstruction and collapsed parcel time-series

White matter surfaces and cortical parcellations/neuroanatomical labels (corresponding to the Schaefer 400-parcels/7-networks atlas (Schaefer et al., 2018)) were extracted from each individual T1-weighted MRI with FreeSurfer 5.1.0

(https://surfer.nmr.mgh.harvard.edu/). The surfaces were imported into MATLAB and aligned from native- to sensor-space using a previously calculated transformation for MRI-MEG co-localization. Next, dipole sources were reconstructed using Fieldtrip's *ft_sourceanalysis* algorithm. First, the forward operator was calculated with the subfunction *ft_prepare_leadfield* for a sourcemodel consisting of 10k to 14k dipole sources placed at the vertices of the white matter surface with an inter-dipole distance of ~7 mm. Second, the inverse operator was computed using minimum norm estimation (MNE) as implemented in *minimumnormestimate*, which uses a regularized noise-covariance-based estimation (here, $\lambda = 0.11$) of brain activity based on dynamic statistical parametric maps (dSPM) (Dale et al., 2000). The estimated dipole sources were then collapsed into Schaefer's 400 parcels after applying a procedure of *fidelity weighting* to minimize the contribution of spurious inter-areal interactions (Siebenhühner et al., 2020). Fidelity weights were calculated by estimating each vertex's fidelity as follows:

(1) Dipole sources were assigned to the nearest parcel (n = 400) and arranged in array form:

$$\begin{bmatrix} P_1 \\ P_2 \\ P_3 \\ \vdots \\ P_{400} \end{bmatrix} = \begin{bmatrix} \{s_1^1 & s_2^1 & s_3^1 & \cdots & s_m^1\} \\ \{s_1^2 & s_2^2 & s_3^2 & \cdots & s_n^2\} \\ \{s_1^3 & s_2^3 & s_3^3 & \cdots & s_o^3\} \\ \vdots & \vdots & \vdots & \ddots & \vdots \\ \{s_1^{400} & s_2^{400} & s_3^{400} & \cdots & s_p^{400}\} \end{bmatrix} \quad (1)$$

where s_k^l represents the *k*th dipole source assigned to parcel P_l. Note the different number of dipole sources on each parcel $\{m, n, o, \dots, p\}$.

(2) 400 parcel time-series (of 10,000 samples) $\{x^1(t), x^2(t), x^3(t), \dots, x^{400}(t)\}$ were simulated using uncorrelated Morlet-filtered white noise. Next, the simulated *parcel* time-series were converted to simulated *source* time-series by assigning each simulated parcel time-series to all the dipole sources within that parcel:

$$\begin{bmatrix} \{s_1^1 & s_2^1 & s_3^1 & \cdots & s_m^1\} \\ \{s_1^2 & s_2^2 & s_3^2 & \cdots & s_n^2\} \\ \{s_1^3 & s_2^3 & s_3^3 & \cdots & s_o^3\} \\ \vdots & \vdots & \vdots & \ddots & \vdots \\ \{s_1^{400} & s_2^{400} & s_3^{400} & \cdots & s_p^{400}\} \end{bmatrix} = \begin{bmatrix} \{x_1^1(t) & x_2^1(t) & x_3^1(t) & \cdots & x_m^1(t)\} \\ \{x_1^2(t) & x_2^2(t) & x_3^2(t) & \cdots & x_n^2(t)\} \\ \{x_1^3(t) & x_2^3(t) & x_3^3(t) & \cdots & x_o^3(t)\} \\ \vdots & \vdots & \vdots & \ddots & \vdots \\ \{x_1^{400}(t) & x_2^{400}(t) & x_3^{400}(t) & \cdots & x_p^{400}(t)\} \end{bmatrix} \quad (2)$$

where $x_1^l(t) = x_2^l(t) = x_3^l(t) = \cdots = x_k^l(t)$.

(3) The *simulated* source time-series were projected to sensor-space using the forward operator, and back-projected to source-space using the inverse operator, yielding a set of *estimated* source time-series:

$$\begin{bmatrix} \{\hat{x}_1^1(t) & \hat{x}_2^1(t) & \hat{x}_3^1(t) & \cdots & \hat{x}_m^1(t)\} \\ \{\hat{x}_1^2(t) & \hat{x}_2^2(t) & \hat{x}_3^2(t) & \cdots & \hat{x}_n^2(t)\} \\ \{\hat{x}_1^3(t) & \hat{x}_2^3(t) & \hat{x}_3^3(t) & \cdots & \hat{x}_o^3(t)\} \\ \vdots & \vdots & \vdots & \ddots & \vdots \\ \{\hat{x}_1^{400}(t) & \hat{x}_2^{400}(t) & \hat{x}_3^{400}(t) & \cdots & \hat{x}_p^{400}(t)\} \end{bmatrix} \tag{3}$$

Eq. (2) is considered the ground truth for Eq. (3), and accordingly, any differences between them are attributed to source-leakage effects during inverse modeling.

(4) Fidelity weights were calculated for every dipole source s_k^l as the correlation between its *simulated* $x_k^l(t)$ and its *estimated* $\hat{x}_k^l(t)$ source time-series:

$$Fid_W_k^l = sign\left(real\left(cPLV_k^l\right)\right) * real(cPLV_k^l)^2 \tag{4}$$

$$cPLV_k^l = \frac{1}{N}\sum_{t=1}^{N} e^{j\left(\theta_{x_k^l(t)} - \theta_{\hat{x}_k^l(t)}\right)} \tag{5}$$

where $cPLV$ is the complex phase-locking value (Lachaux et al., 1999; S. Palva & Palva, 2012), j is the imaginary unit, and $\theta_{x_k^l(t)}$ is the phase of the signal $x_k^l(t)$.

(5) The fidelity weights were multiplied by the inverse operator and collapsed into Schaefer's 400 parcels to obtain a *parcel fidelity-weighted* inverse operator, which was then applied to the sensor-space time-series (n = 306) to reconstruct parcel time-series (n = 400) with improved accuracy.

Long-range temporal correlations (LRTCs)

The linear DFA has been widely used as a quantitative measure of LRTCs in narrow-band time-series irrespective of whether they arise from stationary processes or not (Peng et al., 1995). The resulting scaling exponent α is a measure of the autocorrelation properties of a signal, i.e., $\alpha < 0.5$: anti-correlated, $\alpha \approx 0.5$: uncorrelated, and $0.5 < \alpha < 1$: correlated.

We used MATLAB scripts imported from the Neurophysiological Biomarker Toolbox (NBT) (https://www.nitrc.org/projects/nbt/) to quantify LRTCs. For each participant, scaling exponents were estimated from parcel time-series, which were narrow-band filtered using a bank of 32 Morlet wavelets (width parameter $m = 5$) log-equidistant within

a bandwidth of 2−90 Hz. For each wavelet frequency, the amplitude envelopes of the narrow-band parcel time-series were extracted and passed to NBT's *nbt_Scaling_DFA*. First, a set of N = 52 window sizes were defined on a log10 scale, ranging from 0.08 to 120 seconds. Second, the cumulative sum of each (demeaned) signal was calculated (the signal profile $g(t)$). Then, for each window size $n \epsilon N$, the signal profile was divided into w windows of length $n \cdot F_s$ samples (with 50% overlap) that were cleared of linear trends, $q_w(t) = g_w(t) - trend(g_w(t))$. Finally, the fluctuation function $F(n)$ was calculated as the averaged root mean square across all windows w of size n:

$$F(n) = \sqrt{mean(RMS(q_w(t)))} \tag{6}$$

This procedure yielded a set of fluctuation functions $F(n)$ for each window size $n \in N$ that were then plotted in a log-log scale. For each Morlet frequency, the scaling exponent α was calculated as the slope of the power-law $F(n) \propto n$ across the adjusted fitting interval (via robust bi-square fitting). Here, the fitting interval included window sizes from 2−25 seconds (as opposed to 0.08−120 seconds) to avoid the influence of filtering artifacts on the scaling exponent estimation.

Functional excitation-inhibition ratio (fE/I)

Bruining and colleagues (Bruining et al., 2020) developed a method to estimate the *f*E/I using simulated data that reproduced the statistical properties of the amplitude fluctuations found in human neuronal oscillations. In their study, *f*E/I−estimated from LRTCs and spectral power−was found similar to the structural E/I of a given network, i.e., to the number of excitatory-to-excitatory synapses divided by the number of inhibitory-to-excitatory synapses. We used custom MATLAB scripts to implement this method as follows: (i) parcel time-series were wavelet-filtered into 32 narrow-band signals (see Long range temporal correlations (LRTCs)) and their amplitude envelopes were extracted; (ii) the cumulative sum of each (demeaned) signal was calculated (the signal profile); (iii) the signal profile was divided by its mean amplitude in fixed windows of 40 cycles, to remove the effect of the original signal magnitude; (iv) each normalized signal profile window was linearly detrended; (v) the standard deviation was calculated for each window to get the windowed-normalized fluctuation function $w_nF(t)$; (vi) mean windowed amplitudes ($wAmp$) were estimated (as in iii); (vii) the Pearson correlation between $w_nF(t)$ and $wAmp$ was calculated, that is, $corr(w_nF(t), wAmp)$; and (viii) *f*E/I values were quantified as $fE/I = 1 - corr(w_nF(t), wAmp)$, so that *f*E/I

= 1 means balanced E/I, *f*E/I < 1 means inhibition dominant, and *f*E/I > 1 means excitation dominant.

Classification model

To test the ability of LRTCs and *f*E/I estimates to correctly discriminate NC, SCD and MCI participants we used the kNN classification algorithm (parameter $k = 15$) with a set of functional (LRTCs and *f*E/I) and structural (bilateral MTL volumes) features. The kNN is a non-parametric supervised learning procedure which uses the concept of proximity and a voting procedure, by which an individual is assigned the most common category among their k - nearest neighbors in the feature space. Three independent classifiers were implemented to account for the binary problems determined by the diagnostic groups included in the study (i.e., NC vs. MCI, NC vs. SCD, and SCD vs. MCI). The initial set of features included:

- 56 functional features, i.e. LRTCs and *f*E/I estimates in Schaefer's 7 networks (i.e., FPN, DMN, DAN, Lim, VAN, SM, Vis), in theta (4-7 Hz), alpha (7-12 Hz), beta (12-30 Hz), and gamma (30-45 Hz) frequency bands;

- 6 structural features (i.e., bilateral MTL volumes: hippocampi, parahippocampi, and entorhinal cortices);

arranged so that each example (trial) represents one different subject (the structure is outlined in Fig.S3a).

Data dimensionality was reduced by applying the *feature selection* algorithm (mRMR; (Ding & Peng, 2005; Radovic et al., 2017)) to select a minimal-optimal subset of 15 features for each of the three binary problems (see Fig. 6). To counteract the negative effects of possible anomalous patterns on the learning procedure, the trials used for feature selection were previously passed through an outlier detection procedure, so that trials including values ≥ 3 scaled median absolute deviations away from the related feature's median, have been temporarily discarded. Once the features were selected, rejected trials were re-introduced in the dataset and classification was conducted using all trials and leave-one-out cross-validation to test model performance. For each of the classifiers the optimal cut-off value was defined as the point on the AUC where the product of sensitivity and specificity was maximized. We used *Shapley additive explanations* (SHAP) (Lundberg & Lee, 2017) to explore the contributions of the different features to the predictions, with the *extension to kernelSHAP* algorithm to

account for feature interdependency (Aas et al., 2021).We then repeated the classification discarding the functional features related to frequency bands other than alpha and beta.

The classifications carried out with the kNN have been repeated using the SVM method (using a Gaussian kernel).

Statistical analysis

The statistical significance of between-group differences was examined at two levels, i.e., subject-wise (as in Fig. 2c) and parcel-wise (as in Fig. 3a). At either level, we used the non-parametric ANOVA (Kruskal-Wallis) test when the statistical comparison was conducted between three groups (NC, SCD, and MCI), and the Wilcoxon Rank-Sum test for post hoc pairwise comparisons (NC-SCD, NC-MCI, SCD-MCI). We performed multiple comparison correction via FDR estimation with $Q = 10\%$ for subject-wise and $Q = 20\%$ for parcel-wise statistics. Similarly, the stats for correlation coefficients (Spearman or Pearson; mentioned in text, where employed) between two measures (e.g., in Fig. 4f, g) or between data from two modalities (Fig. 5a, b) are computed using paired t-test and FDR accounted for multiple comparisons.

Tables

Table 1. Demographic and neuropsychological measurements for each group in the cross-sectional dataset.

	NC	SCD	MCI
N	116	85	142
Age	70.21 ± 4.38**	72.16 ± 5.29*	73.45 ± 5.44*
Gender (M/F)	39/77	18/67	50/92
BNT [0 60]	54.25 ± 6.56**	49.81 ± 7.62**	44.22 ± 9.09**
Digit Span_F [0 16]	8.85 ± 2.56*	8.43 ± 1.96*	6.97 ± 1.93**
Digit Span_B [0 14]	6.04 ± 2.01**	5.29 ± 1.78**	4.27 ± 1.42**
LMIU [0 75]	40.90 ± 9.62**	33.54±11.48**	15.86 ± 8.84**
LMDU [0 75]	25.41 ± 7.49**	19.48 ± 8.72**	5.78 ± 6.60**
LMIT [0 75]	16.98 ± 2.58**	15.21 ± 3.57**	10 ± 4.14**
LMDT [0 75]	11.20 ± 1.99**	9.76 ± 2.96**	4.08 ± 3.56**
Fluency Phonologic	14.93 ± 4.56**	11.49 ± 3.74**	8.34 ± 4.06**
Fluency Semantic	17.31 ± 3.64**	15.39 ± 2.84**	12.01 ± 3.37**
L hippocampal volume	0.0026 ± 0.0003**	0.0024 ± 0.0004**	0.0022 ± 0.0004**
L hippocampal volume (reg)	0.0026 ± 0.0003*	0.0024 ± 0.0004*	0.0022 ± 0.0004**
R hippocampal volume	0.0025 ± 0.0003*	0.0025 ± 0.0004*	0.0022 ± 0.0004**
L parahippocampal volume	0.0014 ± 0.0003*	0.0014 ± 0.0003*	0.0012 ± 0.0002**
R parahippocampal volume	0.0013 ± 0.0002**	0.0012 ± 0.0002**	0.0011 ± 0.0002**
R parahippocampal volume (reg)	0.0013 ± 0.0002*	0.0012 ± 0.0002*	0.0011 ± 0.0002**
L entorhinal volume	0.0013 ± 0.0002*	0.0013 ± 0.0003*	0.0011 ± 0.0003**
R entorhinal volume	0.0013 ± 0.0002*	0.0012 ± 0.0003*	0.0010 ± 0.0003**

[1] The table shows (unless noted) mean ± standard deviation values of the demographic and neuropsychological measurements. *denotes statistical significance (independent samples t-test, $p < 0.05$). Asterisk color indicates the groups compared (e.g., an orange asterisk in the NC column denotes NC-MCI significant differences). Due to significant differences in age, we also looked at group differences in all variables after regressing out age confounds, which resulted in same statistics except for few mentioned explicitly with keyword: '(reg)'. NC, neurotypical control; SCD, subjective cognitive decline; MCI, mild cognitive impairment; M, male; F, female; BNT, Boston Naming Test; F, forward; B, backward; LMIU, Logical Memory Immediate Units; LMDU, Logical Memory Delayed Units; LMIT, Logical Memory Immediate Thematic; LMDL, Logical Memory Delayed Thematic; L, left; R, right.

Table 2. Demographic and clinical measurements for each group in the longitudinal dataset (pre- and post-sessions).

	sMCI	**pMCI**
N	22	23
Gender (M/F)	8/14	9/14
Age (pre-session)	71.73 ± 5.20	73.70 ± 3.40
Age (post-session)	73.05 ± 4.85	75.87 ± 3.55
MMSE (pre-session)	27.45 ± 2.28	25.79 ± 3.34
MMSE (post-session)	26.73 ± 3.06	23.41 ± 4.24

[1] The table shows (unless noted) mean ± standard deviation values of the demographic and clinical measurements. sMCI, stable mild cognitive impairment; pMCI, progressive mild cognitive impairment; M, male; F, female; MMSE, Mini-Mental State Examination.

References

Aas, K., Jullum, M., & Løland, A. (2021). Explaining individual predictions when features are dependent: More accurate approximations to Shapley values. *Artificial Intelligence*, *298*, 103502. https://doi.org/10.1016/j.artint.2021.103502

Albert, M. S., DeKosky, S. T., Dickson, D., Dubois, B., Feldman, H. H., Fox, N. C., Gamst, A., Holtzman, D. M., Jagust, W. J., Petersen, R. C., Snyder, P. J., Carrillo, M. C., Thies, B., & Phelps, C. H. (2011). The diagnosis of mild cognitive impairment due to Alzheimer's disease: recommendations from the National Institute on Aging-Alzheimer's Association workgroups on diagnostic guidelines for Alzheimer's disease. *Alzheimer's & Dementia : The Journal of the Alzheimer's Association*, *7*(3), 270–279. https://doi.org/10.1016/j.jalz.2011.03.008

Ambrad Giovannetti, E., & Fuhrmann, M. (2019). Unsupervised excitation: GABAergic dysfunctions in Alzheimer's disease. *Brain Research*, *1707*, 216–226. https://doi.org/10.1016/j.brainres.2018.11.042

Babiloni, C., Blinowska, K., Bonanni, L., Cichocki, A., De Haan, W., Del Percio, C., Dubois, B., Escudero, J., Fernández, A., Frisoni, G., Guntekin, B., Hajos, M., Hampel, H., Ifeachor, E., Kilborn, K., Kumar, S., Johnsen, K., Johannsson, M., Jeong, J., … Randall, F. (2020). What electrophysiology tells us about Alzheimer's disease: a window into the synchronization and connectivity of brain neurons. *Neurobiology of Aging*, *85*, 58–73. https://doi.org/https://doi.org/10.1016/j.neurobiolaging.2019.09.008

Babiloni, C., Del Percio, C., Caroli, A., Salvatore, E., Nicolai, E., Marzano, N., Lizio, R., Cavedo, E., Landau, S., Chen, K., Jagust, W., Reiman, E., Tedeschi, G., Montella, P., De Stefano, M., Gesualdo, L., Frisoni, G. B., & Soricelli, A. (2016). Cortical sources of resting state EEG rhythms are related to brain hypometabolism in subjects with Alzheimer's disease: an EEG-PET study. *Neurobiology of Aging*, *48*, 122–134. https://doi.org/https://doi.org/10.1016/j.neurobiolaging.2016.08.021

Babiloni, C., Del Percio, C., Lizio, R., Noce, G., Cordone, S., Lopez, S., Soricelli, A., Ferri, R., Pascarelli, M. T., Nobili, F., Arnaldi, D., Famà, F., Aarsland, D., Orzi, F., Buttinelli, C., Giubilei, F., Onofrj, M., Stocchi, F., Stirpe, P., … De Pandis, M. F. (2017). Abnormalities of Cortical Neural Synchronization Mechanisms in Subjects with Mild Cognitive Impairment due to Alzheimer's and Parkinson's Diseases: An EEG Study. *Journal of Alzheimer's Disease*, *59*, 339–358. https://doi.org/10.3233/JAD-160883

Bai, Y., Hu, Y., Wu, Y., Zhu, Y., He, Q., Jiang, C., Sun, L., & Fan, W. (2012). A prospective, randomized, single-blinded trial on the effect of early rehabilitation on daily activities and motor function of patients with hemorrhagic stroke. *Journal of Clinical Neuroscience*, *19*(10), 1376–1379. https://doi.org/10.1016/j.jocn.2011.10.021

Beggs, J. M., & Plenz, D. (2003). Neuronal Avalanches in Neocortical Circuits. *The Journal of Neuroscience*, *23*(35), 11167 LP – 11177. https://doi.org/10.1523/JNEUROSCI.23-35-11167.2003

Benton, A., Hamsher, S., & Sivan, A. (1983). *Multilingual aphasia examination: manual of instructions*. [Iowa City] : Dept. of Neurology and Psychology, University of Iowa.

Blinowska, K. J., Rakowski, F., Kaminski, M., De Vico Fallani, F., Del Percio, C., Lizio, R., & Babiloni, C. (2017). Functional and effective brain connectivity for discrimination between Alzheimer's patients and healthy individuals: A study on resting state EEG rhythms. *Clinical Neurophysiology : Official Journal of the International Federation of Clinical Neurophysiology*, *128*(4), 667–680. https://doi.org/10.1016/j.clinph.2016.10.002

Brassen, S., & Adler, G. (2003). Short-term effects of acetylcholinesterase inhibitor treatment on EEG and memory performance in Alzheimer patients: an open, controlled trial. *Pharmacopsychiatry*, *36*(6), 304–308. https://doi.org/10.1055/s-2003-45118

Bruining, H., Hardstone, R., Juarez-Martinez, E. L., Sprengers, J., Avramiea, A.-E., Simpraga, S., Houtman, S. J., Poil, S.-S., Dallares, E., Palva, S., Oranje, B., Matias Palva, J., Mansvelder, H. D., & Linkenkaer-Hansen, K. (2020). Measurement of excitation-inhibition ratio in autism spectrum disorder using critical brain dynamics. *Scientific Reports*, *10*(1), 9195. https://doi.org/10.1038/s41598-020-65500-4

Buckner, R. L., Sepulcre, J., Talukdar, T., Krienen, F. M., Liu, H., Hedden, T., Andrews-Hanna, J. R., Sperling, R. A., & Johnson, K. A. (2009). Cortical Hubs Revealed by Intrinsic Functional Connectivity: Mapping, Assessment of Stability, and Relation to Alzheimer's Disease. *The Journal of Neuroscience*, *29*(6), 1860 LP – 1873. https://doi.org/10.1523/JNEUROSCI.5062-08.2009

Busche, M. A., & Konnerth, A. (2016). Impairments of neural circuit function in Alzheimer's disease. *Philosophical Transactions of the Royal Society of London. Series B, Biological Sciences*, *371*(1700), 20150429. https://doi.org/10.1098/rstb.2015.0429

Chialvo, D. R. (2010). Emergent complex neural dynamics. *Nature Physics*, *6*(10), 744–750. https://doi.org/10.1038/nphys1803

Cocchi, L., Gollo, L. L., Zalesky, A., & Breakspear, M. (2017). Criticality in the brain: A synthesis of neurobiology, models and cognition. *Progress in Neurobiology*, *158*, 132–152. https://doi.org/https://doi.org/10.1016/j.pneurobio.2017.07.002

Corbetta, M., Patel, G., & Shulman, G. L. (2008). The reorienting system of the human brain: from environment to theory of mind. *Neuron*, *58*(3), 306–324. https://doi.org/10.1016/j.neuron.2008.04.017

Dale, A. M., Liu, A. K., Fischl, B. R., Buckner, R. L., Belliveau, J. W., Lewine, J. D., & Halgren, E. (2000). Dynamic statistical parametric mapping: combining fMRI and MEG for high-resolution imaging of cortical activity. *Neuron*, *26*(1), 55–67. https://doi.org/10.1016/s0896-6273(00)81138-1

de Haan, W., van Straaten, E. C. W., Gouw, A. A., & Stam, C. J. (2017). Altering neuronal excitability to preserve network connectivity in a computational model of Alzheimer's disease. *PLOS Computational Biology*, *13*(9), e1005707. https://doi.org/10.1371/journal.pcbi.1005707

Ding, C., & Peng, H. (2005). Minimum redundancy feature selection from microarray gene expression data. *Journal of Bioinformatics and Computational Biology*, *3*(2), 185–205. https://doi.org/10.1142/s0219720005001004

Fell, J., & Axmacher, N. (2011). The role of phase synchronization in memory processes. *Nature Reviews. Neuroscience*, *12*(2), 105–118. https://doi.org/10.1038/nrn2979

Folstein, M. F., Folstein, S. E., & McHugh, P. R. (1975). "Mini-mental state". A practical method for grading the cognitive state of patients for the clinician. *Journal of Psychiatric Research*, *12(3)*(3), 189–198. https://doi.org/10.1016/0022-3956(75)90026-6

Fries, P. (2015). Rhythms for Cognition: Communication through Coherence. *Neuron*, *88*(1), 220–235. https://doi.org/10.1016/j.neuron.2015.09.034

Fuscà, M., Siebenhühner, F., Wang, S. H., Myrov, V., Arnulfo, G., Nobili, L., Palva, J. M., & Palva, S. (2022). Brain criticality predicts individual synchronization levels in humans. *BioRxiv*, 2022.11.24.517800. https://doi.org/10.1101/2022.11.24.517800

Garcia-Marin, V., Blazquez-Llorca, L., Rodriguez, J.-R., Boluda, S., Muntane, G., Ferrer, I., &

Defelipe, J. (2009). Diminished perisomatic GABAergic terminals on cortical neurons adjacent to amyloid plaques. *Frontiers in Neuroanatomy*, *3*, 28. https://doi.org/10.3389/neuro.05.028.2009

Haldeman, C., & Beggs, J. M. (2005). Critical Branching Captures Activity in Living Neural Networks and Maximizes the Number of Metastable States. *Phys. Rev. Lett.*, *94*(5), 58101. https://doi.org/10.1103/PhysRevLett.94.058101

Hardstone, R., Poil, S.-S., Schiavone, G., Jansen, R., Nikulin, V. V, Mansvelder, H. D., & Linkenkaer-Hansen, K. (2012). Detrended fluctuation analysis: a scale-free view on neuronal oscillations. *Frontiers in Physiology*, *3*, 450. https://doi.org/10.3389/fphys.2012.00450

Jack, C. R., Knopman, D. S., Jagust, W. J., Petersen, R. C., Weiner, M. W., Aisen, P. S., Shaw, L. M., Vemuri, P., Wiste, H. J., Weigand, S. D., Lesnick, T. G., Pankratz, V. S., Donohue, M. C., & Trojanowski, J. Q. (2013). Tracking pathophysiological processes in Alzheimer's disease: an updated hypothetical model of dynamic biomarkers. *The Lancet. Neurology*, *12*(2), 207–216. https://doi.org/10.1016/S1474-4422(12)70291-0

Jelic, V., Johansson, S. E., Almkvist, O., Shigeta, M., Julin, P., Nordberg, A., Winblad, B., & Wahlund, L. O. (2000). Quantitative electroencephalography in mild cognitive impairment: longitudinal changes and possible prediction of Alzheimer's disease. *Neurobiology of Aging*, *21*(4), 533–540. https://doi.org/10.1016/s0197-4580(00)00153-6

Jeong, J. (2004). EEG dynamics in patients with Alzheimer's disease. *Clinical Neurophysiology : Official Journal of the International Federation of Clinical Neurophysiology*, *115*(7), 1490–1505. https://doi.org/10.1016/j.clinph.2004.01.001

Jessen, F., Amariglio, R. E., van Boxtel, M., Breteler, M., Ceccaldi, M., Chételat, G., Dubois, B., Dufouil, C., Ellis, K. A., van der Flier, W. M., Glodzik, L., van Harten, A. C., de Leon, M. J., McHugh, P., Mielke, M. M., Molinuevo, J. L., Mosconi, L., Osorio, R. S., Perrotin, A., … Wagner, M. (2014). A conceptual framework for research on subjective cognitive decline in preclinical Alzheimer's disease. *Alzheimer's & Dementia : The Journal of the Alzheimer's Association*, *10*(6), 844–852. https://doi.org/10.1016/j.jalz.2014.01.001

Kaplan, E., Goodglas, H., & Weintraub, S. (2001). *The Boston Naming Test* (2nd ed.). Lippincott Williams & Wilkins.

Klaus, A., Yu, S., & Plenz, D. (2011). Statistical Analyses Support Power Law Distributions Found in Neuronal Avalanches. *PLOS ONE*, *6*(5), e19779. https://doi.org/10.1371/journal.pone.0019779

Klimesch, W., Sauseng, P., & Hanslmayr, S. (2007). EEG alpha oscillations: the inhibition-timing hypothesis. *Brain Research Reviews*, *53*(1), 63–88. https://doi.org/10.1016/j.brainresrev.2006.06.003

Lachaux, J. P., Rodriguez, E., Martinerie, J., & Varela, F. J. (1999). Measuring phase synchrony in brain signals. *Human Brain Mapping*, *8*(4), 194–208. https://doi.org/10.1002/(sici)1097-0193(1999)8:4<194::aid-hbm4>3.0.co;2-c

Levina, A., Herrmann, J. M., & Geisel, T. (2009). Phase Transitions towards Criticality in a Neural System with Adaptive Interactions. *Phys. Rev. Lett.*, *102*(11), 118110. https://doi.org/10.1103/PhysRevLett.102.118110

Li, W., Wang, M., Zhu, W., Qin, Y., Huang, Y., & Chen, X. (2016). Simulating the Evolution of Functional Brain Networks in Alzheimer's Disease: Exploring Disease Dynamics from the Perspective of Global Activity. *Scientific Reports*, *6*(1), 34156. https://doi.org/10.1038/srep34156

Linkenkaer-Hansen, K., Nikouline, V. V, Palva, J. M., & Ilmoniemi, R. J. (2001). Long-Range

Temporal Correlations and Scaling Behavior in Human Brain Oscillations. *The Journal of Neuroscience*, *21*(4), 1370 LP – 1377. https://doi.org/10.1523/JNEUROSCI.21-04-01370.2001

Lojo-Seoane, C., Facal, D., Guàrdia-Olmos, J., Pereiro, A. X., & Juncos-Rabadán, O. (2018). Effects of Cognitive Reserve on Cognitive Performance in a Follow-Up Study in Older Adults With Subjective Cognitive Complaints. The Role of Working Memory. In *Frontiers in Aging Neuroscience* (Vol. 10, p. 189). https://www.frontiersin.org/article/10.3389/fnagi.2018.00189

López-Sanz, D., Bruña, R., Garcés, P., Martín-Buro, M. C., Walter, S., Delgado, M. L., Montenegro, M., López Higes, R., Marcos, A., & Maestú, F. (2017). Functional Connectivity Disruption in Subjective Cognitive Decline and Mild Cognitive Impairment: A Common Pattern of Alterations. *Frontiers in Aging Neuroscience*, *9*, 109. https://doi.org/10.3389/fnagi.2017.00109

López, M. E., Turrero, A., Delgado, M. L., Rodríguez-Rojo, I. C., Arrazola, J., Barabash, A., Maestú, F., & Fernández, A. (2017). APOE ε4 Genotype and Cognitive Reserve Effects on the Cognitive Functioning of Healthy Elders. *Dementia and Geriatric Cognitive Disorders*, *44*(5–6), 328–342. https://doi.org/10.1159/000481852

Lundberg, S. M., & Lee, S. I. (2017). A Unified Approach to Interpreting Model Predictions. *Advances in Neural Information Processing Systems*, *2017-Decem*, 4766–4775. https://doi.org/10.48550/arxiv.1705.07874

Maestú, F., de Haan, W., Busche, M. A., & DeFelipe, J. (2021). Neuronal excitation/inhibition imbalance: core element of a translational perspective on Alzheimer pathophysiology. *Ageing Research Reviews*, *69*, 101372. https://doi.org/10.1016/j.arr.2021.101372

Maestú, F., & Fernández, A. (2020). Role of Magnetoencephalography in the Early Stages of Alzheimer Disease. *Neuroimaging Clinics of North America*, *30*(2), 217–227. https://doi.org/10.1016/j.nic.2020.01.003

Maestú, F., Peña, J.-M., Garcés, P., González, S., Bajo, R., Bagic, A., Cuesta, P., Funke, M., Mäkelä, J. P., Menasalvas, E., Nakamura, A., Parkkonen, L., López, M. E., del Pozo, F., Sudre, G., Zamrini, E., Pekkonen, E., Henson, R. N., & Becker, J. T. (2015). A multicenter study of the early detection of synaptic dysfunction in Mild Cognitive Impairment using Magnetoencephalography-derived functional connectivity. *NeuroImage: Clinical*, *9*, 103–109. https://doi.org/https://doi.org/10.1016/j.nicl.2015.07.011

McKhann, G. M., Knopman, D. S., Chertkow, H., Hyman, B. T., Jack, C. R. J., Kawas, C. H., Klunk, W. E., Koroshetz, W. J., Manly, J. J., Mayeux, R., Mohs, R. C., Morris, J. C., Rossor, M. N., Scheltens, P., Carrillo, M. C., Thies, B., Weintraub, S., & Phelps, C. H. (2011). The diagnosis of dementia due to Alzheimer's disease: recommendations from the National Institute on Aging-Alzheimer's Association workgroups on diagnostic guidelines for Alzheimer's disease. *Alzheimer's & Dementia : The Journal of the Alzheimer's Association*, *7*(3), 263–269. https://doi.org/10.1016/j.jalz.2011.03.005

Meder, A., Liepelt-Scarfone, I., Sulzer, P., Berg, D., Laske, C., Preische, O., Desideri, D., Zipser, C. M., Salvadore, G., Tatikola, K., Timmers, M., & Ziemann, U. (2021). Motor cortical excitability and paired-associative stimulation-induced plasticity in amnestic mild cognitive impairment and Alzheimer's disease. *Clinical Neurophysiology : Official Journal of the International Federation of Clinical Neurophysiology*, *132*(9), 2264–2273. https://doi.org/10.1016/j.clinph.2021.01.011

Nakamura, A., Cuesta, P., Kato, T., Arahata, Y., Iwata, K., Yamagishi, M., Kuratsubo, I., Kato, K., Bundo, M., Diers, K., Fernández, A., Maestú, F., & Ito, K. (2017). Early functional network alterations in asymptomatic elders at risk for Alzheimer's disease. *Scientific Reports*, *7*(1), 6517. https://doi.org/10.1038/s41598-017-06876-8

Nikulin, V. V, Jönsson, E. G., & Brismar, T. (2012). Attenuation of long-range temporal correlations in the amplitude dynamics of alpha and beta neuronal oscillations in patients with schizophrenia. *NeuroImage*, *61*(1), 162–169. https://doi.org/10.1016/j.neuroimage.2012.03.008

Oldfield, R. C. (1971). The assessment and analysis of handedness: the Edinburgh inventory. *Neuropsychologia*, *9*(1), 97–113. https://doi.org/10.1016/0028-3932(71)90067-4

Oostenveld, R., Fries, P., Maris, E., & Schoffelen, J.-M. (2011). FieldTrip: Open source software for advanced analysis of MEG, EEG, and invasive electrophysiological data. *Computational Intelligence and Neuroscience*, *2011*, 156869. https://doi.org/10.1155/2011/156869

Palva, J. M., Zhigalov, A., Hirvonen, J., Korhonen, O., Linkenkaer-Hansen, K., & Palva, S. (2013). Neuronal long-range temporal correlations and avalanche dynamics are correlated with behavioral scaling laws. *Proceedings of the National Academy of Sciences*, *110*(9), 3585 LP – 3590. https://doi.org/10.1073/pnas.1216855110

Palva, S., & Palva, J. M. (2012). Discovering oscillatory interaction networks with M/EEG: challenges and breakthroughs. *Trends in Cognitive Sciences*, *16*(4), 219–230. https://doi.org/10.1016/j.tics.2012.02.004

Palva, S., & Palva, J. M. (2018). Roles of Brain Criticality and Multiscale Oscillations in Temporal Predictions for Sensorimotor Processing. *Trends in Neurosciences*, *41*(10), 729–743. https://doi.org/10.1016/j.tins.2018.08.008

Peng, C. K., Havlin, S., Stanley, H. E., & Goldberger, A. L. (1995). Quantification of scaling exponents and crossover phenomena in nonstationary heartbeat time series. *Chaos (Woodbury, N.Y.)*, *5*(1), 82–87. https://doi.org/10.1063/1.166141

Pini, L. (2023). Brain network modulation in Alzheimer's disease: clinical phenotypes and windows of opportunity. *Neural Regeneration Research*, *18*(1), 115–116. https://doi.org/10.4103/1673-5374.340410

Pinto, D. J., Jones, S. R., Kaper, T. J., & Kopell, N. (2003). Analysis of state-dependent transitions in frequency and long-distance coordination in a model oscillatory cortical circuit. *Journal of Computational Neuroscience*, *15*(2), 283–298. https://doi.org/10.1023/a:1025825102620

Plenz, D., & Thiagarajan, T. C. (2007). The organizing principles of neuronal avalanches: cell assemblies in the cortex? *Trends in Neurosciences*, *30*(3), 101–110. https://doi.org/https://doi.org/10.1016/j.tins.2007.01.005

Poil, S.-S., Hardstone, R., Mansvelder, H. D., & Linkenkaer-Hansen, K. (2012). Critical-State Dynamics of Avalanches and Oscillations Jointly Emerge from Balanced Excitation/Inhibition in Neuronal Networks. *The Journal of Neuroscience*, *32*(29), 9817 LP – 9823. https://doi.org/10.1523/JNEUROSCI.5990-11.2012

Power, J. D., & Petersen, S. E. (2013). Control-related systems in the human brain. *Current Opinion in Neurobiology*, *23*(2), 223–228. https://doi.org/10.1016/j.conb.2012.12.009

Priesemann, V., Wibral, M., Valderrama, M., Pröpper, R., Le Van Quyen, M., Geisel, T., Triesch, J., Nikolić, D., & Munk, M. H. J. (2014). Spike avalanches in vivo suggest a driven, slightly subcritical brain state. In *Frontiers in Systems Neuroscience* (Vol. 8). https://www.frontiersin.org/article/10.3389/fnsys.2014.00108

Pusil, S., López, M. E., Cuesta, P., Bruña, R., Pereda, E., & Maestú, F. (2019). Hypersynchronization in mild cognitive impairment: the "X" model. *Brain : A Journal of Neurology*, *142*(12), 3936–3950. https://doi.org/10.1093/brain/awz320

Radovic, M., Ghalwash, M., Filipovic, N., & Obradovic, Z. (2017). Minimum redundancy maximum relevance feature selection approach for temporal gene expression data. *BMC*

Bioinformatics, *18*(1), 9. https://doi.org/10.1186/s12859-016-1423-9

Ramírez-Toraño, F., Abbas, K., Bruña, R., Marcos de Pedro, S., Gómez-Ruiz, N., Barabash, A., Pereda, E., Marcos, A., López-Higes, R., Maestu, F., & Goñi, J. (2021). A Structural Connectivity Disruption One Decade before the Typical Age for Dementia: A Study in Healthy Subjects with Family History of Alzheimer's Disease. *Cerebral Cortex Communications*, *2*(4), tgab051. https://doi.org/10.1093/texcom/tgab051

Ranasinghe, K. G., Verma, P., Cai, C., Xie, X., Kudo, K., Gao, X., Lerner, H., Mizuiri, D., Strom, A., Iaccarino, L., La Joie, R., Miller, B. L., Gorno-Tempini, M. L., Rankin, K. P., Jagust, W. J., Vossel, K., Rabinovici, G. D., Raj, A., & Nagarajan, S. S. (2022). Altered excitatory and inhibitory neuronal subpopulation parameters are distinctly associated with tau and amyloid in Alzheimer's disease. *ELife*, *11*. https://doi.org/10.7554/eLife.77850

Schaefer, A., Kong, R., Gordon, E. M., Laumann, T. O., Zuo, X.-N., Holmes, A. J., Eickhoff, S. B., & Yeo, B. T. T. (2018). Local-Global Parcellation of the Human Cerebral Cortex from Intrinsic Functional Connectivity MRI. *Cerebral Cortex*, *28*(9), 3095–3114. https://doi.org/10.1093/cercor/bhx179

Schoffelen, J.-M., & Gross, J. (2009). Source connectivity analysis with MEG and EEG. *Human Brain Mapping*, *30*(6), 1857–1865. https://doi.org/10.1002/hbm.20745

Shew, W. L., Yang, H., Petermann, T., Roy, R., & Plenz, D. (2009). Neuronal Avalanches Imply Maximum Dynamic Range in Cortical Networks at Criticality. *The Journal of Neuroscience*, *29*(49), 15595 LP – 15600. https://doi.org/10.1523/JNEUROSCI.3864-09.2009

Shumbayawonda, E., López-Sanz, D., Bruña, R., Serrano, N., Fernández, A., Maestú, F., & Abásolo, D. (2020). Complexity changes in preclinical Alzheimer's disease: An MEG study of subjective cognitive decline and mild cognitive impairment. *Clinical Neurophysiology*, *131*, 437–445.

Siebenhühner, F., Wang, S. H., Arnulfo, G., Lampinen, A., Nobili, L., Palva, J. M., & Palva, S. (2020). Genuine cross-frequency coupling networks in human resting-state electrophysiological recordings. *PLOS Biology*, *18*(5), e3000685. https://doi.org/10.1371/journal.pbio.3000685

Siegel, M., Donner, T. H., & Engel, A. K. (2012). Spectral fingerprints of large-scale neuronal interactions. *Nature Reviews. Neuroscience*, *13*(2), 121–134. https://doi.org/10.1038/nrn3137

Simola, J., Zhigalov, A., Morales-Muñoz, I., Palva, J. M., & Palva, S. (2017). Critical dynamics of endogenous fluctuations predict cognitive flexibility in the Go/NoGo task. *Scientific Reports*, *7*(1), 2909. https://doi.org/10.1038/s41598-017-02750-9

Singer, W. (1999). Temporal Coherence: A Versatile Code for the Definition of Relations. *Neuron*, *24*, 49–65. https://doi.org/10.1016/B978-012370880-9.00287-5

Smallwood, J., Bernhardt, B. C., Leech, R., Bzdok, D., Jefferies, E., & Margulies, D. S. (2021). The default mode network in cognition: a topographical perspective. *Nature Reviews. Neuroscience*, *22*(8), 503–513. https://doi.org/10.1038/s41583-021-00474-4

Smith, R. J., Ombao, H. C., Shrey, D. W., & Lopour, B. A. (2020). Inference on Long-Range Temporal Correlations in Human EEG Data. *IEEE Journal of Biomedical and Health Informatics*, *24*(4), 1070–1079. https://doi.org/10.1109/JBHI.2019.2936326

Stam, C. J., Nolte, G., & Daffertshofer, A. (2007). Phase lag index: assessment of functional connectivity from multi channel EEG and MEG with diminished bias from common sources. *Human Brain Mapping*, *28*(11), 1178–1193. https://doi.org/10.1002/hbm.20346

Taulu, S., & Hari, R. (2009). Removal of magnetoencephalographic artifacts with temporal

signal-space separation: demonstration with single-trial auditory-evoked responses. *Human Brain Mapping*, *30*(5), 1524–1534. https://doi.org/10.1002/hbm.20627

Thut, G., Miniussi, C., & Gross, J. (2012). The functional importance of rhythmic activity in the brain. *Current Biology : CB*, *22*(16), R658-63. https://doi.org/10.1016/j.cub.2012.06.061

Toker, D., Pappas, I., Lendner, J. D., Frohlich, J., Mateos, D. M., Muthukumaraswamy, S., Carhart-Harris, R., Paff, M., Vespa, P. M., Monti, M. M., Sommer, F. T., Knight, R. T., & D'Esposito, M. (2022). Consciousness is supported by near-critical slow cortical electrodynamics. *Proceedings of the National Academy of Sciences*, *119*(7), e2024455119. https://doi.org/10.1073/pnas.2024455119

Wechsler, D. (2004). *Escala de memoria de Wechsler-III: manual técnico*. TEA Ediciones.

Womelsdorf, T., Ardid, S., Everling, S., & Valiante, T. A. (2014). Burst Firing Synchronizes Prefrontal and Anterior Cingulate Cortex during Attentional Control. *Current Biology*, *24*(22), 2613–2621. https://doi.org/https://doi.org/10.1016/j.cub.2014.09.046